COMMUNICATIONS IN COMPUTATIONAL PHYSICS
Vol. **3**, No. 3, pp. 603-640

Commun. Comput. Phys.
March 2008

Modelling of Propagating Shear Waves in Biotissue Employing an Internal Variable Approach to Dissipation

H. T. Banks*and Nicholas S. Luke

Center for Research in Scientific Computation, North Carolina State University, Raleigh, NC 27695-8205, USA.

Received 7 February 2007; Accepted (in revised version) 28 July 2007

Communicated by Wei Cai

Available online 30 October 2007

Abstract. The ability to reliably detect coronary artery disease based on the acoustic noises produced by a stenosis can provide a simple, non-invasive technique for diagnosis. Current research exploits the shear wave fields in body tissue to detect and analyze coronary stenoses. The methods and ideas outlined in earlier efforts [6] including a mathematical model utilizing an internal strain variable approximation to the quasi-linear viscoelastic constitutive equation proposed by Fung in [19] is extended here. As an initial investigation, a homogeneous two-dimensional viscoelastic geometry is considered. Being uniform in θ, this geometry behaves as a one dimensional model, and the results generated from it are compared to the one dimensional results from [6]. To allow for different assumptions on the elastic response, several variations of the model are considered. A statistical significance test is employed to determine if the more complex models are significant improvements. After calibrating the model with a comparison to previous findings, more complicated geometries are considered. Simulations involving a heterogeneous geometry with a uniform ring running through the original medium, a θ-dependent model which considers a rigid partial occlusion formed along the inner radius of the geometry, and a model which combines the ring and occlusion are presented.

AMS subject classifications: 74D10, 35L45, 62P10

Key words: Viscoelasticity, partial differential equations, shear waves, biotissue.

1 Introduction

Coronary artery disease (CAD), also known as coronary heart disease (CHD), is the most common form of heart disease. The National Institute of Health estimates that approximately seven million Americans suffer from the disease, and roughly 500,000 deaths per

*Corresponding author. *Email addresses:* htbanks@ncsu.edu (H. T. Banks), nsluke@ncsu.edu (N. S. Luke)

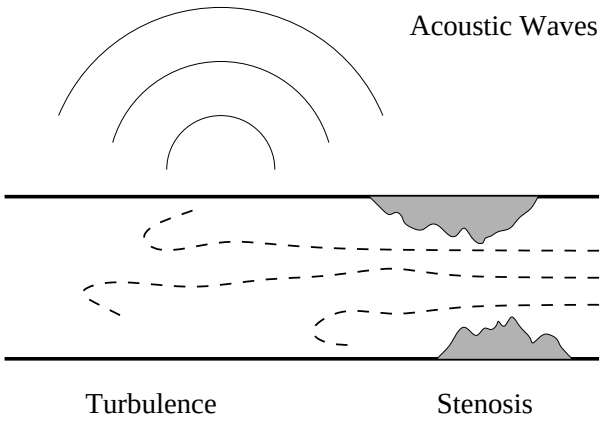

Figure 1: Turbulent blood flow generated by a stenosis.

year can be attributed to CHD [3]. It is caused by atherosclerosis, the gradual buildup of plaque (cholesterol, calcium, and platelets) within the artery. This accumulation of plaque, known as a *stenosis*, restricts the flow of blood, leading to a decrease in the oxygen supply to the heart muscle. The end result of an arterial stenosis is permanent damage to the heart muscle, possibly leading to death. Because CAD affects so many people in the United States, and worldwide, its detection and treatment is a matter of significant interest.

Current detection techniques include the angiogram which is a reliable, yet expensive, invasive technique and also prone to interobserver variability (see e.g., [20,33]). Ultra-fast CT techniques are also employed; this is a non-invasive imaging technique effective in detecting and scoring the severity of calcium deposits in the coronary arteries. Unfortunately, CT testing equipment is very expensive, and it only detects calcium deposits and not the soft plaques that make up many of the most dangerous lesions.

A plausible alternative to the angiogram and CT scan for detection of stenoses utilizes the detection of acoustic waves propagating from the stenosis. It is well known that arterial stenoses produce sounds due to turbulent blood flow in partially occluded arteries. In principle, turbulent normal wall forces exist at and downstream from an arterial stenosis. These wall forces, which are extremely small, exert a pressure on the wall of the artery which then causes a small displacement in the surrounding body tissue (see Fig. 1). The vibrations of the surrounding body tissues, which occur in two forms, a compressional wave and a shear wave, produce sounds [39]. In larger arteries such as the carotid arteries, these acoustic sounds can be detected by physicians using a stethoscope. However, detecting acoustic signals in smaller arteries deep inside the body has proved difficult for two reasons: these acoustic noises attenuate significantly as they travel through the intervening tissues, and many complex sounds within the body can overwhelm conventional acoustic detection systems.

During the late 1990's, MedAcoustics Inc., a company financed by venture capital,

developed and patented a polyvinyldifluoride (PVDF) array of piezoelectric thin film accelerometer sensor elements. These sensors are band-limited, so as to filter out irrelevant signals (e.g., heartbeat) and so, when placed on a person's acoustic window (located on the chest surface), the array has the ability to detect acoustic shear waves due to arterial stenoses. Utilizing this technology, doctors would have an inexpensive means of deciding whether or not an angiography is needed. As the hardware was designed to collect acceleration data from the wave propagation at the chest wall, it did not provide any insight into how the waves traveled through the chest cavity. A mathematical framework was needed to model the wave propagation from the stenosis to the chestwall, and allow for the eventual detection of stenoses. Initial developments of the mathematical model were presented in [6].

The idea of utilizing acoustic waves in biological and medical applications is not new. In fact, there has been much research conducted in the field of transient elastography, a method which utilizes acoustic waves and sensors to map an image of selected tissue (see, e.g., [18, 21, 38]). In [16] the authors discuss the ability to detect tumors in breast tissue. Similarly the authors of [42] consider tumor detectability in liver tissue. An inverse problem methodology involving data from transient elastography is presented in [24, 25, 32].

The formulation of constitutive equations is a nontrivial difficulty that arises when considering biological tissue as a medium. It is well accepted that body soft tissue medium behaves like a viscoelastic medium [19, 29, 34, 43]. However, there are several techniques available to incorporate viscoelasticity into a model. In [5, 27], the authors propose that applications of fractional calculus be used in viscoelastic modelling. A mathematical framework that examines several methods for dealing with viscoelasticity (in lung tissue) is presented in [41]. Finally, Fung introduced a quasi-linear viscoelastic constitutive law in [19]. While there are numerous ways to represent the relaxation function in Fung's law, the work presented in this paper is based on the internal variable approach discussed in [6].

In Section 2 of this presentation, we outline a derivation of the model for an annular geometry. We begin with the equations of motion, and detail the formulation (including different variations) of relevant constitutive equations. We examine the validity of our model in Section 4 by comparing its generated results to data generated in the one dimensional geometry investigations of [6]. In particular, we present a comparison of results generated by each variation of our model with the one dimensional data presented in [6]. A statistical significance test is employed in Section 5 to examine the significance of extra parameters involved in the more complex models.

In Section 6 we present several simulations produced using the model for different geometries motivated by practical interests. We consider heterogeneities by introducing a uniform ring in the middle of the annular geometry. Dependence on θ is introduced by considering a rigid occlusion located along a portion of the inner radius of the annulus. Finally, we examine a geometry which combines the annular heterogeneity and inner occlusion. We close with concluding remarks and possible future directions for needed research.

2 Model formulation

2.1 Physical geometry of the model

Although the motivation of this problem involves the detection of stenoses within the human body, several complexities exist with the consideration of the chest cavity. The medium within the chest cavity is heterogeneous. The shape of the chest cavity is generally elliptical, but varies between subjects. For these reasons, we consider, for our initial efforts, a more simplistic geometry motivated by the experiments at MedAcoustics.

The simplified physical geometry is a cylindrical gel mold. The synthetic gel of which the geometry is comprised has material properties similar to those of soft tissues. A surgical tube which mimics an arterial vein with stenosis, passes axisymmetrically through the center of the mold. A source disturbance (representative of the disturbance caused by stenosis) is generated within the tube. Shear waves propagate through the gel, and the shear acceleration is measured (by sensors) at the outer surface of the gel.

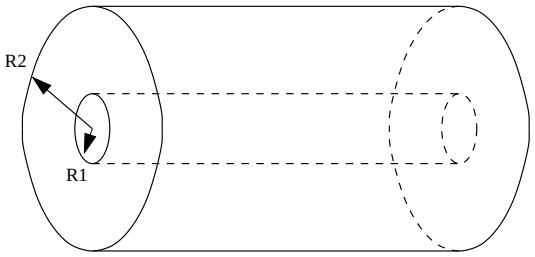

Figure 2: Illustration of the physical geometry considered in our modelling efforts.

Let R_1 and R_2 be the inner radius and outer radius, respectively, of the annular configuration of gel (see Fig. 2). We assume that the source disturbance is time dependent, has only a radial component, and the disturbance is a pure shear force. The outer surface of the gel is a free surface and the gel is initially at rest.

Because we are interested in modelling the wave propagation from the inner radius to the outer radius, we neglect here the axial direction, and concentrate on a cross section of the cylindrical mold. This cross sectional area takes the shape of a circle and thus it will be beneficial to derive our model using polar coordinates. A full three dimensional model in which the stenosis depends on location along the cylindrical axis can be readily based on the model we employ here.

2.2 The equations of motion

From conservation of mass, we have the continuity equation, in polar coordinates

$$\frac{\partial \rho}{\partial t}+\frac{\partial \rho v_1}{\partial r}+\frac{1}{r}\frac{\partial \rho v_2}{\partial \theta}+\frac{\rho v_1}{r}=0, \tag{2.1}$$

where v_1,v_2 are the velocities in the radial and tangential directions, respectively. Conservation of momentum takes the form (here the σ_{ij} are the usual stresses associated with the radial and tangential directions)

$$\frac{\partial \rho v_1}{\partial t} = -\frac{\partial \rho v_1^2}{\partial r} - \frac{1}{r}\frac{\partial \rho v_2 v_1}{\partial \theta} - \frac{1}{r}(\rho v_1^2 - \rho v_2^2) + \frac{\partial \sigma_{11}}{\partial r} + \frac{1}{r}\frac{\partial \sigma_{21}}{\partial \theta} + \frac{1}{r}(\sigma_{11} - \sigma_{22}), \tag{2.2}$$

$$\frac{\partial \rho v_2}{\partial t} = -\frac{\partial \rho v_1 v_2}{\partial r} - \frac{1}{r}\frac{\partial \rho v_2^2}{\partial \theta} - \frac{1}{r}(\rho v_1 v_2 + \rho v_2 v_1) + \frac{\partial \sigma_{12}}{\partial r} + \frac{1}{r}\frac{\partial \sigma_{22}}{\partial \theta} + \frac{1}{r}(\sigma_{12} + \sigma_{21}). \tag{2.3}$$

Utilizing the continuity equation (2.1) in the left sides of the momentum equations (2.2) and (2.3), we arrive at the following equations of motion for a continuum

$$\rho\left(\frac{\partial v_1}{\partial t} + v_1\frac{\partial v_1}{\partial r} + \frac{v_2}{r}\frac{\partial v_1}{\partial \theta} - \frac{v_2^2}{r}\right) = \frac{\partial \sigma_{11}}{\partial r} + \frac{1}{r}\frac{\partial \sigma_{21}}{\partial \theta} + \frac{1}{r}(\sigma_{11} - \sigma_{22}),$$

$$\rho\left(\frac{\partial v_2}{\partial t} + v_1\frac{\partial v_2}{\partial r} + \frac{v_2}{r}\frac{\partial v_2}{\partial \theta} - \frac{v_1 v_2}{r}\right) = \frac{\partial \sigma_{12}}{\partial r} + \frac{1}{r}\frac{\partial \sigma_{22}}{\partial \theta} + \frac{1}{r}(\sigma_{12} + \sigma_{21}).$$

Because we are dealing with only small displacements, the higher order terms are negligible; thus we ignore them and use the substitutions $v_1 = \frac{\partial u_1}{\partial t}$ and $v_2 = \frac{\partial u_2}{\partial t}$ to obtain

$$\rho\frac{\partial^2 u_1}{\partial t^2} = \frac{\partial \sigma_{11}}{\partial r} + \frac{1}{r}\frac{\partial \sigma_{21}}{\partial \theta} + \frac{1}{r}(\sigma_{11} - \sigma_{22}), \tag{2.4}$$

$$\rho\frac{\partial^2 u_2}{\partial t^2} = \frac{\partial \sigma_{12}}{\partial r} + \frac{1}{r}\frac{\partial \sigma_{22}}{\partial \theta} + \frac{1}{r}(\sigma_{12} + \sigma_{21}). \tag{2.5}$$

For a more detailed derivation of these equations of motion, see [31].

3 Formulation of the constitutive equations

Having presented the equations of motion, we need to formulate the constitutive equations to complete our model. Constitutive equations typically quantify the relationship between the stresses to which a material is subjected and the strain response. To formulate a set of constitutive equations, we begin with the generalized quasi-linear viscoelastic model proposed by Fung [19],

$$S_{ij}(t) = \int_{-\infty}^{t} G_{ijkl}(t-\tau)\frac{\partial S_{kl}^{(e)}[\bar{E}(\tau)]}{\partial \tau}d\tau,$$

where S_{ij} is the Kirchhoff stress tensor, $\bar{E}$ is the Green's strain tensor, G_{ijkl} is the reduced relaxation function, and $S_{kl}^{(e)}$ is the "elastic" stress tensor.

Since its introduction, this quasi-linear viscoelastic (QLV) theory has been applied to several tissues including, among others, tendons [22], ligaments [45], articular cartilage under tension [44], heart valves [37], papillary muscle [35], and smooth muscle [36]. A

benefit to using the QLV theory is that, unlike simpler models for viscoelasticity, it allows for the consideration of a continuous spectrum of relaxation times and frequencies. The QLV theory has been shown capable of modelling relaxation, creep, and hysteresis within viscoelastic materials. Fung and others in the modelling efforts listed above have shown that the QLV theory works well for fitting stress-strain relationships numerically to experimental data.

While Fung's theory is mainly used for stress-strain fits, we are interested in using it in a full dynamical model. Unfortunately, the QLV, as presented by Fung, leads to challenging computations when incorporated into dynamical partial differential equations. We turn to a conceptual alternative to Fung's kernel in which we use a parameter dependent kernel with a continuum distribution of parameters and internal variables. This approach has been used successfully in electromagnetics [9, 10] as well as in other viscoelastic problems [12–15]. If, in this context, we employ a finite combination of δ measures, we arrive at a finite dimensional summation of exponential functions as our approximation kernel. Theoretical support for convergence of this approximation can be found in [7, 14]. This form of the internal variable approach was also used in [6], in which the authors have shown that a weighted sum of appropriately decaying exponentials when included in the dynamic partial differential equations approximates Fung's kernel fairly well at the system response or solution level. Further details of our internal variable approach and the associated approximations are presented in Section 3.3.

3.1 Elastic response

We consider the elastic stress tensor $S_{ij}^{(e)}$ corresponding to the strain tensor $\bar{E}$; it is a function of the strain components E_{ij}, which, in polar coordinates can be expressed as [17]

$$\begin{aligned} E_{11} &= \frac{\partial u_1}{\partial r}, \\ E_{22} &= \frac{1}{r}\frac{\partial u_2}{\partial \theta} + \frac{u_1}{r}, \\ E_{21} &= E_{12} = \frac{1}{r}\frac{\partial u_1}{\partial \theta} + \frac{\partial u_2}{\partial r} - \frac{u_2}{r}. \end{aligned}$$

We recall that $S_{ij}^{(e)}$ is defined to be the stress that is reached instantaneously when the strains are suddenly increased from 0 to E_{ij}.

Following the one-dimensional arguments presented in [19], we assume that the "elastic" responses can be approximated by pseudo-elastic stresses, where the pseudo-elastic stresses take the form of the derivative of a pseudo-strain energy function $(\rho_o W)$ with respect to components E_{ij} of the strain tensor, i.e.,

$$S_{ij}^{(e)} \approx S_{ij} = \frac{\partial(\rho_0 W)}{\partial E_{ij}}.$$

In two dimensional experiments involving skin tissue, Fung [19] chose the following form for the pseudo-strain-energy function

$$\begin{aligned}\rho_0 W^{(2)} = &\frac{1}{2}(\alpha_1 E_{11}^2+\alpha_2 E_{22}^2+\alpha_3 E_{12}^2+\alpha_3 E_{21}^2+2\alpha_4 E_{11}E_{22})\\ &+\frac{c}{2}exp(a_1 E_{11}^2+a_2 E_{22}^2+a_3 E_{12}^2+a_3 E_{21}^2+2a_4 E_{11}E_{22}\\ &+\gamma_1 E_{11}^3+\gamma_2 E_{22}^3+\gamma_4 E_{11}^2 E_{22}+\gamma_5 E_{11}E_{22}^2),\end{aligned} \tag{3.1}$$

where the α's, a's, γ's, and c are constants. According to Fung, the pseudo-strain energy function for arterial walls and lung tissue also takes the form of (3.1). In Fung's experiments, investigators fixed $E_{12}=E_{21}=0$; they also found that the higher order γ terms can be neglected without a significant loss of accuracy. In this case, (3.1) simplifies to

$$\rho_0 W^{(2)} = f(\bar{\alpha},\bar{E})+c(\exp[F(\bar{a},\bar{E})]), \tag{3.2}$$

where

$$\begin{aligned}f(\bar{\alpha},\bar{E}) &= \alpha_1 E_{11}^2+\alpha_2 E_{22}^2+\alpha_3 E_{12}^2+\alpha_3 E_{21}^2+2\alpha_4 E_{11}E_{22},\\ F(\bar{a},\bar{E}) &= a_1 E_{11}^2+a_2 E_{22}^2+a_3 E_{12}^2+a_3 E_{21}^2+2a_4 E_{11}E_{22}.\end{aligned}$$

Note that $f(\bar{\alpha},\bar{E})$, and $F(\bar{a},\bar{E})$ are of the same form, and only differ by the values of the coefficients $\bar{\alpha}=(\alpha_1,\alpha_2,\alpha_3,\alpha_4)^T$ and $\bar{a}=(a_1,a_2,a_3,a_4)^T$.

It should be noted that the first term in (3.2) was introduced because the data analyzed in [19] appeared biphasic. The second term expresses the behavior of the material at high stresses and the first term remedies the situation at a lower stress level. If we are concerned mainly with higher stresses and strains in the physiological range, and do not care for great accuracy at very small stress levels, then we might disregard the first term in (3.2) and obtain

$$\rho_0 W^{(2)} \approx c(\exp[F(\bar{a},\bar{E})]). \tag{3.3}$$

The elastic responses for the full (to second order using (3.2)) pseudo-elastic strain energy function will take the form

$$\begin{aligned}S_{11}^{(e)} &= \frac{\partial \rho_0 W^{(2)}}{\partial E_{11}} = 2(\alpha_1 E_{11}+\alpha_4 E_{22})+2c(a_1 E_{11}+a_4 E_{22})\exp(a_1 E_{11}^2+a_2 E_{22}^2\\ &\quad +a_3 E_{12}^2+a_3 E_{21}^2+2a_4 E_{11}E_{22}),\\ S_{12}^{(e)} &= \frac{\partial \rho_0 W^{(2)}}{\partial E_{12}} = 2\alpha_3 E_{12}+2ca_3 E_{12}\exp(a_1 E_{11}^2+a_2 E_{22}^2+a_3 E_{12}^2+a_3 E_{21}^2+2a_4 E_{11}E_{22}),\\ S_{21}^{(e)} &= \frac{\partial \rho_0 W^{(2)}}{\partial E_{21}} = 2\alpha_3 E_{21}+2ca_3 E_{21}\exp(a_1 E_{11}^2+a_2 E_{22}^2+a_3 E_{12}^2+a_3 E_{21}^2+2a_4 E_{11}E_{22}),\\ S_{22}^{(e)} &= \frac{\partial \rho_0 W^{(2)}}{\partial E_{22}} = 2(\alpha_4 E_{11}+\alpha_2 E_{22})+2c(a_4 E_{11}+a_2 E_{22})\exp(a_1 E_{11}^2+a_2 E_{22}^2\\ &\quad +a_3 E_{12}^2+a_3 E_{21}^2+2a_4 E_{11}E_{22}).\end{aligned}$$

This full version of the elastic response involves 9 unknown parameters, c, α_1, α_2, α_3, α_4, a_1, a_2, a_3, and a_4. Depending on the attributes which we wish to capture in our model, we can approximate the pseudo-strain energy function and resulting elastic responses accordingly. We now present different elastic response model simplifications that will be considered subsequently in our presentation. These models will be labeled models ER1, ER2, and ER3, respectively, and are defined as follows.

ER1 In this model, we neglect the small stress term $f(\bar{\alpha},\bar{E})$. We use the pseudo strain energy function (3.2), and set $E_{12}=E_{21}\approx 0$ (as did Fung in [19]), to obtain

$$\begin{aligned}
S_{11}^{(e)} &= 2c(a_1E_{11}+a_4E_{22})\exp(a_1E_{11}^2+a_2E_{22}^2+2a_4E_{11}E_{22}),\\
S_{12}^{(e)} &= S_{21}^{(e)}=0,\\
S_{22}^{(e)} &= 2c(a_4E_{11}+a_2E_{22})\exp(a_1E_{11}^2+a_2E_{22}^2+2a_4E_{11}E_{22}).
\end{aligned}$$

This model involves 4 unknown parameters: c,a_1,a_2, and a_4.

ER2 In this case, we again neglect the small stress term $f(\bar{\alpha},\bar{E})$, and use the pseudo strain-energy function (3.2), with $E_{12}=E_{21}$ no longer assumed negligible, to find

$$\begin{aligned}
S_{11}^{(e)} &= 2c(a_1E_{11}+a_4E_{22})\exp(a_1E_{11}^2+a_2E_{22}^2+2a_3E_{12}^2+2a_4E_{11}E_{22}),\\
S_{12}^{(e)} &= S_{21}^{(e)}=2ca_3E_{12}\exp(a_1E_{11}^2+a_2E_{22}^2+2a_3E_{12}^2+2a_4E_{11}E_{22}),\\
S_{22}^{(e)} &= 2c(a_4E_{11}+a_2E_{22})\exp(a_1E_{11}^2+a_2E_{22}^2+2a_3E_{12}^2+2a_4E_{11}E_{22}).
\end{aligned}$$

This model involves 5 unknown parameters: c,a_1,a_2,a_3, and a_4.

ER3 For the third model, we retain the small stress term $f(\bar{\alpha},\bar{E})$, use the pseudo strain energy function (3.1), and take $E_{12}=E_{21}\approx 0$, which results in

$$\begin{aligned}
S_{11}^{(e)} &= 2(\alpha_1E_{11}+\alpha_4E_{22})+2c(a_1E_{11}+a_4E_{22})\exp(a_1E_{11}^2+a_2E_{22}^2+2a_4E_{11}E_{22}),\\
S_{12}^{(e)} &= S_{21}^{(e)}=0,\\
S_{22}^{(e)} &= 2(\alpha_4E_{11}+\alpha_2E_{22})+2c(a_4E_{11}+a_2E_{22})\exp(a_1E_{11}^2+a_2E_{22}^2+2a_4E_{11}E_{22}).
\end{aligned}$$

This case involves 7 unknown parameters: c,α_1,α_2,α_4,a_1,a_2, and a_4.

3.2 The reduced relaxation function

We next consider the reduced relaxation function tensor G_{ijkl} of rank 4, where the word "reduced" refers to the condition $G_{ijkl}=1$ when $t=0$. If we make the assumption that the material is isotropic [4], then the reduced relaxation function will only have two independent components, and we can rewrite it as

$$G_{ijkl}=\lambda\delta_{ij}\delta_{kl}+\mu(\delta_{ik}\delta_{jl}+\delta_{il}\delta_{jk}). \tag{3.4}$$

Since the assumption of isotropy implies that $S_{kl}^{(e)} = S_{lk}^{(e)}$, we have

$$G_{ijkl}(t-\tau)\frac{\partial}{\partial\tau}S_{kl}^{(e)}(t) = \lambda(t-\tau)\frac{\partial}{\partial\tau}(S_{11}^{(e)}(\tau)+S_{22}^{(e)}(\tau))\delta_{ij}+2\mu(t-\tau)\frac{\partial}{\partial\tau}S_{ij}^{(e)}(\tau).$$

Thus, we can express Fung's generalized viscoelastic relation for isotropic materials as

$$S_{ij}(t) = \int_{-\infty}^{t}\left[\lambda(t-\tau)\frac{\partial}{\partial\tau}(S_{11}^{(e)}(\tau)+S_{22}^{(e)}(\tau))\delta_{ij}+2\mu(t-\tau)\frac{\partial}{\partial\tau}S_{ij}^{(e)}(\tau)\right]d\tau.$$

3.3 The internal variable model approximation

In [6], the authors begin with Fung's one dimensional quasi-linear viscoelastic model

$$\sigma(t) = \int_{-\infty}^{t} G(t-\tau)\frac{\partial}{\partial\tau}\sigma^{(e)}(\lambda(\tau))d\tau,$$

but then adopt an internal variable approach and show that multiple linear internal variable models are equivalent to approximating G by sums involving multiple exponential terms.

We utilize the same methodology in the two dimensional case. We begin by approximating the parameters λ and μ in (3.4) with exponentials, such that

$$\lambda(t) = C_\lambda e^{-\nu_\lambda t}; \quad \mu(t) = C_\mu e^{-\nu_\mu t}.$$

If we define

$$\epsilon_\lambda = \int_{-\infty}^{t}\lambda(t-\tau)\frac{\partial}{\partial\tau}(S_{11}^{(e)}(\tau)+S_{22}^{(e)}(\tau))d\tau,$$
$$\epsilon_\mu^{ij} = \int_{-\infty}^{t}2\mu(t-\tau)\frac{\partial}{\partial\tau}S_{ij}^{(e)}(\tau)d\tau,$$

then $S_{ij} = \epsilon_\lambda\delta_{ij}+\epsilon_\mu^{ij}$, where the dynamics of ϵ_λ and ϵ_μ^{ij} are given by the linear differential equations

$$\frac{d\epsilon_\lambda}{dt} = -\nu_\lambda\epsilon_\lambda + C_\lambda\frac{d}{dt}(S_{11}^{(e)}+S_{22}^{(e)}),$$
$$\frac{d\epsilon_\mu^{ij}}{dt} = -\nu_\mu\epsilon_\mu + 2C_\mu\frac{d}{dt}(S_{ij}^{(e)}).$$

The terms ϵ_λ and ϵ_μ are therefore internal variables analogous to those defined in the one dimensional case in [6]. The generalization of this idea for multiple internal variables is as follows. Define S_{ij} using a sum of internal strain variables, as follows

$$S_{ij} = \delta_{ij}(\epsilon_{\lambda_1}+\epsilon_{\lambda_2}+\cdots)+(\epsilon_{\mu_1}^{ij}+\epsilon_{\mu_2}^{ij}+\cdots).$$

The dynamics of the k^{th} internal variables, $k=1,2,\cdots$, are given by

$$\frac{d\epsilon_{\lambda_k}}{dt}=f_{\lambda_k}(\epsilon_{\lambda_k})+C_{\lambda_k}\frac{d}{dt}(S_{11}^{(e)}+S_{22}^{(e)}),\quad \epsilon_{\lambda_k}(0)=0,$$
$$\frac{d\epsilon_{\mu_k}^{ij}}{dt}=f_{\mu_k}(\epsilon_{\mu_k})^{ij}+2C_{\mu_k}\frac{d}{dt}(S_{ij}^{(e)}),\quad \epsilon_{\mu_k}(0)=0,$$

where f_{λ_k} and f_{μ_k} may be linear or nonlinear functions of ϵ_{λ_k} and ϵ_{μ_k}, respectively. The constants C_{λ_k},C_{μ_k}, and any constants associated with f_{λ_k} and f_{μ_k} are unknown parameters to be determined by comparison with data (either through empirical comparisons and/or inverse problem techniques).

3.4 A generic internal variable based model

Combining the equations of motion and the constitutive equations derived in the previous sections, we can now state succinctly the basic model. The following system of equations represents a general framework for our approximate model

$$\rho\frac{\partial^2 u_1}{\partial t^2}=\frac{\partial}{\partial r}(\epsilon_\lambda+\epsilon_\mu^{11})+\frac{1}{r}\frac{\partial}{\partial\theta}(\epsilon_\mu^{21})+\frac{1}{r}(\epsilon_\mu^{11}-\epsilon_\mu^{22}),$$
$$\rho\frac{\partial^2 u_2}{\partial t^2}=\frac{\partial}{\partial r}(\epsilon_\mu^{12})+\frac{1}{r}\frac{\partial}{\partial\theta}(\epsilon_\lambda+\epsilon_\mu^{22})+\frac{1}{r}(\epsilon_\mu^{12}+\epsilon_\mu^{21}),$$
$$\frac{\partial\epsilon_{\lambda_k}}{\partial t}=-\nu_{\lambda_k}\epsilon_{\lambda_k}+C_{\lambda_k}\frac{\partial}{\partial t}\left(S_{11}^{(e)}+S_{22}^{(e)}\right),$$
$$\frac{\partial\epsilon_{\mu_k}^{11}}{\partial t}=-\nu_{\mu_k}\epsilon_{\mu_k}^{11}+C_{\mu_k}\frac{\partial}{\partial t}\left(S_{11}^{(e)}\right),$$
$$\frac{\partial\epsilon_{\mu_k}^{12}}{\partial t}=-\nu_{\mu_k}\epsilon_{\mu_k}^{12}+C_{\mu_k}\frac{\partial}{\partial t}\left(S_{12}^{(e)}\right),$$
$$\frac{\partial\epsilon_{\mu_k}^{22}}{\partial t}=-\nu_{\mu_k}\epsilon_{\mu_k}^{22}+C_{\mu_k}\frac{\partial}{\partial t}\left(S_{22}^{(e)}\right),\quad k=1,2,\cdots.$$

Initial conditions

We assume that the medium is initially at rest, thus

$$u_1(0,r,\theta)=u_2(0,r,\theta)=v_1(0,r,\theta)=v_2(0,r,\theta)=0,\quad S_{ij}(0,r,\theta)=0.$$

For convenience, we also assume that the internal strain variables are zero at time $t=0$.

Boundary conditions

- *Inner Radius:* The stress (or force) along the inner radius of our model will be governed by the impulse function which represents the disturbance due to the stenosis. Thus

$$\sigma_{ij}(t,R_1,\theta)=f_{ij}(t,R_1,\theta).$$

- *Outer Radius:* The outer radius of the model represents a free surface, so

$$\sigma_{ij}(t,R_2,\theta)=S_{ij}(t,R_2,\theta)=0.$$

This generic model is readily configured to account for the different assumptions for ER1, ER2 or ER3 presented in Section 3.1 by substituting the appropriate expressions for $S_{ij}^{(e)}$.

3.5 Computational models

To numerically integrate the model, we chose to convert it into an equivalent system of first order PDEs. This is accomplished through a series of substitutions. The variables v_1,v_2,w_1,w_2,w_3, and w_4, which are defined below, was used to formulate all computational models. The variables which we used are defined by

$$v_1=\frac{\partial u_1}{\partial t},\quad v_2=\frac{\partial u_2}{\partial t},\quad w_1=\frac{\partial u_1}{\partial r},\quad w_2=\frac{\partial u_1}{\partial \theta},\quad w_3=\frac{\partial u_2}{\partial r},\quad w_4=\frac{\partial u_2}{\partial \theta},$$

$$F(\bar{a},\bar{w},\bar{u},r)=a_1w_1^2+a_2\left(\frac{w_4+u_1}{r}\right)^2+2a_3\left(\frac{w_2-u_2}{r}+w_3\right)^2+2a_4w_1\left(\frac{w_4+u_1}{r}\right),$$

where $\bar{a}=(a_1,a_2,a_3,a_4)^T$, $\bar{w}=(w_1,w_2,w_3,w_4)^T$, and $\bar{u}=(u_1,u_2)^T$. The state variables z_i vary, depending on the assumptions made in the model formulation, but maintain a similar form in each variation of the model. For example, in the simplest case, ER1-1ISV, the z_i variables are defined by

$$z_1=\epsilon_\lambda-2cC_\lambda\exp[F(\bar{a},\bar{w},\bar{u},r)]\left[(a_1+a_4)w_1+(a_2+a_4)\frac{1}{r}(w_4+u_1)\right],$$

$$z_2=\epsilon_\mu^{11}-4cC_\mu\exp[F(\bar{a},\bar{w},\bar{u},r)]\left[a_1w_1+\frac{a_4}{r}(w_4+u_1)\right],$$

$$z_3=\epsilon_\mu^{22}-4cC_\mu\exp[F(\bar{a},\bar{w},\bar{u},r)]\left[a_4w_1+\frac{a_2}{r}(w_4+u_1)\right].$$

We consider four variations of our model: ER1-1ISV employs the first elastic response assumption with one internal strain variable, ER2-1ISV uses the second elastic response with one internal strain variable, ER3-1ISV utilizes the third elastic response with one internal strain variable, and ER1-2ISV, entails the first elastic response with 2 internal strain variables. For details of the formulation of each of our model variations, we refer readers to [31].

4 Calibration of the model

Once the models have been formulated, we wish to investigate their utility, differences and appropriateness. By considering a homogeneous material geometry which is independent of θ, we reduce the two dimensional problem to a one dimensional problem. In this special case, we should be able to reproduce the acceleration results presented in [6], depicted here in Fig. 3.

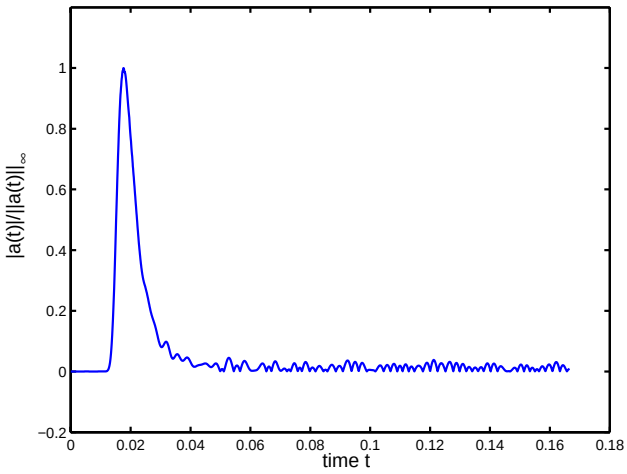

Figure 3: Normalized acceleration data employed in [6].

4.1 Computational methods

We utilize the MacCormack finite difference scheme (a two-step integration scheme-see [26, 40]) to numerically integrate each system. The first step utilizes forward differences and is followed by a step of backward differences. The scheme is known to be second order in space and time (we demonstrate this below). While the forward discretization may be unstable for positive eigenvalues of A and the second, corrector step is unstable for negative eigenvalues, the overall combined scheme is known to be stable and of second order due to the cancelations of the truncation errors of each step [23].

To update boundary terms, we use direction cosines, also known as the method of boundary characteristics [23]. If we define U to be the vector of state variables, then we can rewrite the first order system in matrix-vector notation in the form

$$U_t = AU_r + BU_\theta + Q,$$

where A is the matrix of coefficients corresponding to U_r, B is the matrix of coefficients corresponding to U_θ, and Q is a vector of terms that do not involve any derivatives. For example, if we consider the simplest model, ER1-1ISV, we have the following matrix for A,

$$A = \begin{bmatrix} 0 & 0 & 0 & 0 & 0 & 0 & 0 & 0 & 0 \\ 0 & 0 & 0 & 0 & 0 & 0 & 0 & 0 & 0 \\ 0 & 0 & 0 & 0 & 0 & 0 & 0 & 0 & 0 \\ 0 & 0 & 0 & 0 & 0 & 0 & 0 & 0 & 0 \\ 0 & 0 & 0 & 0 & 0 & 0 & 0 & 0 & 0 \\ b_1\rho^{-1} & 0 & \rho^{-1} & \rho^{-1} & 0 & 0 & 0 & b_2\rho^{-1} & b_3\rho^{-1} \\ 0 & 0 & 0 & 0 & 0 & 0 & 0 & 0 & 0 \\ 0 & 0 & 0 & 0 & 0 & 1 & 0 & 0 & 0 \\ 0 & 0 & 0 & 0 & 0 & 0 & 0 & 0 & 0 \end{bmatrix},$$

where $U=(u_1,u_2,z_1,z_2,z_3,v_1,v_2,w_1,w_2)^T$, and b_1, b_2, and b_3 are appropriate functions of w_1,w_4,u_1,r, and the undetermined constants.

To apply the method of direction cosines, we examine the eigenvalues of the matrices A, and B, depending on the boundary being considered. We begin by considering the boundary along the inner and outer radii. To employ direction cosines on these boundaries, we must consider the matrix A. The eigenvalues of the matrix correspond to the characteristics of the problem. If the eigenvalue is positive, the characteristic speed is positive, giving the characteristic a positive slope. If the eigenvalue is negative, then the characteristic has a negative slope, and negative speed. Fig. 4 represents our geometry, and depicts how characteristics with positive and negative speeds (C_+ and C_-, respectively) interact with the inner and outer radius boundaries.

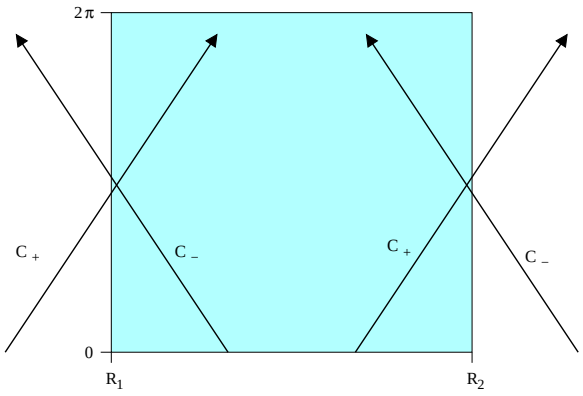

Figure 4: Positive and negative characteristics interacting with domain boundaries.

Along the inner radius, represented by the left boundary in Fig. 4, the characteristic with positive slope points into the domain. This means that information propagates from the boundary, and so the interior points will depend on boundary information. In this case, we must prescribe a physical boundary condition for any characteristics that point into the domain. The characteristic with negative slope points outward from the domain. This implies that the boundary data is dependent on the interior data. For characteristics that point out of the domain, the boundary condition must be updated numerically, based on the interior data.

Revisiting the ER1-1ISV model, one can ascertain that the eigenvalues of the matrix A are $\lambda_A=0,\pm\sqrt{b_2/\rho}$. That is, there is one positive eigenvalue, one negative eigenvalue, and seven eigenvalues which are zero. As explained above, on the inner radius, the positive eigenvalue corresponds to a characteristic which will point into the domain. Thus, we shall have one prescribed physical boundary condition on the inner radius. In order to reproduce the data presented in [6], our physical boundary condition on the inner radius is $w_1(t,R_1,\theta)=f(t)$, where $f(t)$ is the same impulse input function used in [6] and depicted in Fig. 5. Boundary values for the other eight variables are determined from

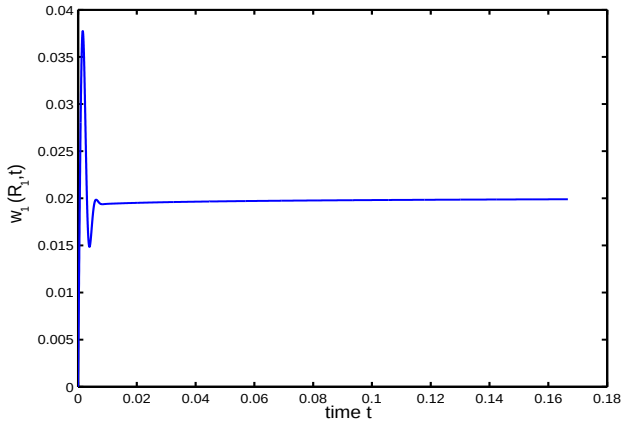

Figure 5: Approximate impulse function w_1 used as boundary data in [6].

interior data points at the previous time step using the second order discretization

$$U^{n+1}=U^n+\Delta t[AU_r+BU_\theta+Q]^n+\frac{1}{2}\Delta t^2[AU_r+BU_\theta+Q]_t^n. \tag{4.1}$$

Examining the outer boundary, we use a similar argument. Since there is only one negative eigenvalue, there can only be one characteristic pointing into the domain, and thus, we can only prescribe one physical boundary condition. We define the physical boundary condition to be

$$w_1(t,R_2,\theta)=\frac{\partial u_1}{\partial r}(t,R_2,\theta)=0.$$

Once again, the other boundary terms are updated using (4.1).

Finally, we can use the periodicity of the geometry to deal with U at $\theta=0$ and $\theta=2\pi$. Since our geometry is circular, we know that the values of our system variables at $\theta=0$ and $\theta=2\pi$ must be the same. This constitutes the final set of boundary conditions for the model ER1-1ISV.

To verify the accuracy of our code, we performed a grid refinement study. We choose exact solutions similar to those utilized in the grid refinement presented in [6]. We define our exact solutions to be

$$u_1(t,r,\theta)=-.2(1-\cos(300t))\left(\frac{r-R_1}{R_2-R_1}\right)^2,$$
$$u_2(t,r,\theta)=-.2(1-\cos(300t))\left(\frac{r-R_1}{R_2-R_1}\right)^2,$$
$$\epsilon_\lambda(t,r,\theta)=\epsilon_\mu^{11}(t,r,\theta)=\epsilon_\mu^{22}(t,r,\theta)=.1\sin(300t)\left(\frac{R_2-r}{R_2-R_1}\right)^2.$$

From our defined exact functions, we are able to calculate $v_1,v_2,w_1,w_2,z_1,z_2,z_3$, and the corresponding forcing functions appropriately. The model is integrated from $t=0$ to $t=1$.

Table 1: Grid Refinement for u_1 and u_2 using ER1-1ISV.

n	$\|\|E_n(u_1)\|\|$	$\frac{\|\|E_n(u_1)\|\|}{\|\|E_{n+1}(u_1)\|\|}$	order	$\|\|E_n(u_2)\|\|$	$\frac{\|\|E_n(u_2)\|\|}{\|\|E_{n+1}(u_2)\|\|}$	order
10	2.0576e-2	4.506	2.1718	2.066e-2	4.5199	2.1762
20	4.5667e-3	4.171	2.0603	4.5717e-3	4.1599	2.0565
40	1.0949e-3	4.106	2.0377	1.0989e-3	4.0582	2.0208
80	2.6665e-4	4.216	2.0759	2.7080e-4	4.0239	2.0086
160	6.3243e-5	4.856	2.2798	6.7298e-5	4.0111	2.0040
320	1.3021e-5			1.6778e-5		

Table 2: Grid Refinement for v_1 and v_2 using ER1-1ISV.

n	$\|\|E_n(v_1)\|\|$	$\frac{\|\|E_n(v_1)\|\|}{\|\|E_{n+1}(v_1)\|\|}$	order	$\|\|E_n(v_2)\|\|$	$\frac{\|\|E_n(v_2)\|\|}{\|\|E_{n+1}(v_2)\|\|}$	order
10	5.6112	4.2625	2.0916	5.6114	4.2626	2.0917
20	1.3164	4.1013	2.0361	1.3164	4.1013	2.0361
40	0.3209	4.0442	2.0159	0.3209	4.0439	2.0157
80	7.9373e-2	4.0216	2.0078	7.9373e-2	4.0203	2.0073
160	1.9735e-2	4.0148	2.0039	1.9735e-2	4.0097	2.0035
320	4.9155e-3			4.9237e-3		

Table 3: Grid Refinement for w_1 using ER1-1ISV.

n	$\|\|E_n(w_1)\|\|$	$\frac{\|\|E_n(w_1)\|\|}{\|\|E_{n+1}(w_1)\|\|}$	order
10	4.3948e-2	3.5196	1.8154
20	1.2471e-2	3.7543	1.9085
40	3.3218e-3	3.9681	1.9884
80	8.3715e-4	4.3307	2.1146
160	1.9330e-4	3.9743	1.9907
320	4.8638e-4		

To perform the refinement, we fix the ratios $\Delta t/\Delta r$ and $\Delta t/\Delta\theta$, run the forward problem, compute the L^∞ error for each model variable, halve the spatial and temporal step sizes, and repeat. The order of accuracy is determined by examining the ratio

$$\ln\left(\frac{||E_n(U_i)||}{||E_{n+1}(U_i)||}\right)\Big/\ln\left(\frac{h_n}{h_n+1}\right),$$

where U_i represents the model variable being examined, and $h_{n,r}$ and $h_{n,\theta}$ are the grid mesh sizes. Tables 1-3 display the grid refinement results for u_1,u_2,v_1,v_2, and w_1, as computed using the ER1-1ISV version of the model.

The grid refinement results displayed in Tables 1-3 verify that our implementation of the MacCormack scheme, with the previously described boundary conditions, is second order accurate, as expected. Grid refinement studies for the other models were conducted, with results analogous to those presented.

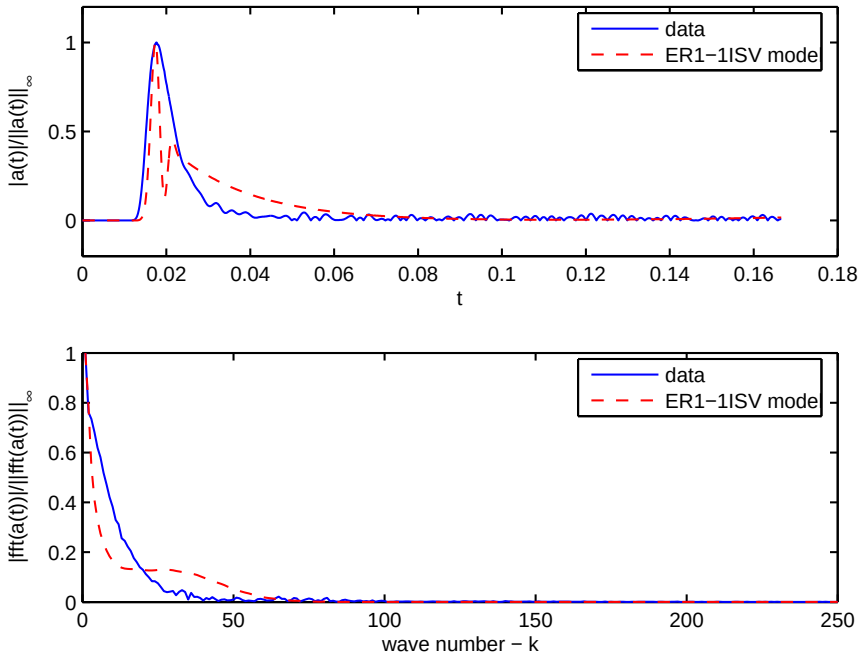

Figure 6: Optimal parameters $(C_\lambda, \nu_\lambda, C_\mu, \nu_\mu) = (6366.919, 768.266, 1.542, 1811.847)$ in model ER1-1ISV vs. data.

4.2 Computational results

We attempted to verify each of the models ability to reproduce the one dimensional acceleration results. We integrated each of our models as described in Section 3.5, and used the results to generate a corresponding acceleration solution for the outer boundary of the geometry. We compared these solutions to the data from [6]. Since our parameters are unknown, we had to seek a set of optimal parameters for each variation of the model, and use the optimal parameter set to generate the solution mentioned above. We used Matlab's *fminsearch* command (an implementation of the Nelder-Mead simplex algorithm) to minimize the difference between the model outputs and the original acceleration data in an ordinary least squares (OLS) formulation, and to identify the optimal parameters.

The optimal parameters for each variation of the model and a comparison of the acceleration data from [6] with the optimized solution from the models presented in Section 3.5 are given in Figs. 6-9 and their captions. Each figure contains two plots. The top plot compares the normalized acceleration data to the normalized solution corresponding to

$$a(t) = \frac{\partial^2 u_1}{\partial t^2}$$

generated by our optimal model, and the bottom plot compares the normalized fast Fourier transform (FFT) of the output data to the normalized fast Fourier transform of our model solution. This plot depicts the wave numbers or frequencies which are excited

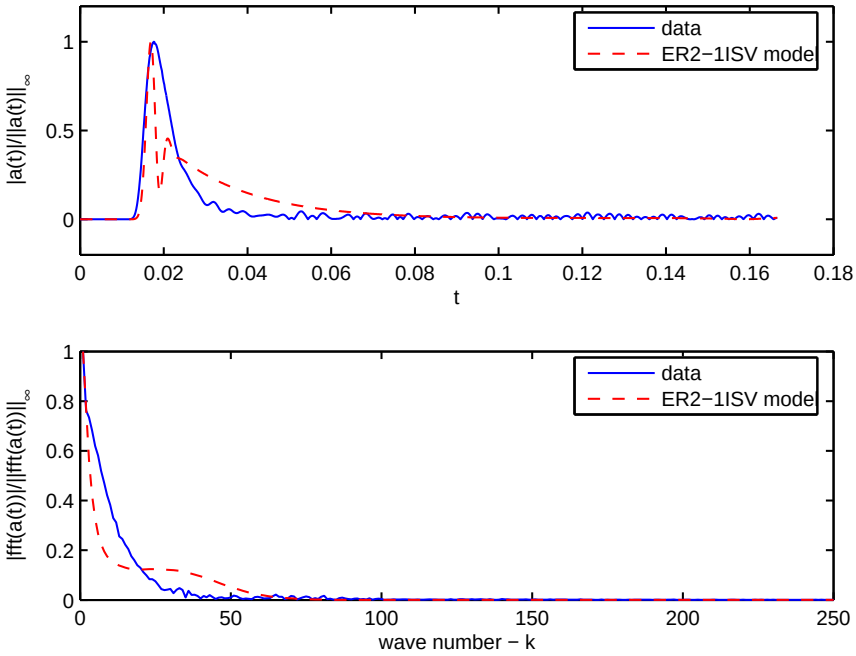

Figure 7: Optimal parameters $(C_\lambda,\nu_\lambda,C_\mu,\nu_\mu,a_3)$=(6683.567,795.935,2.788,3678.888,-1.888) in model ER2-1ISV vs. data.

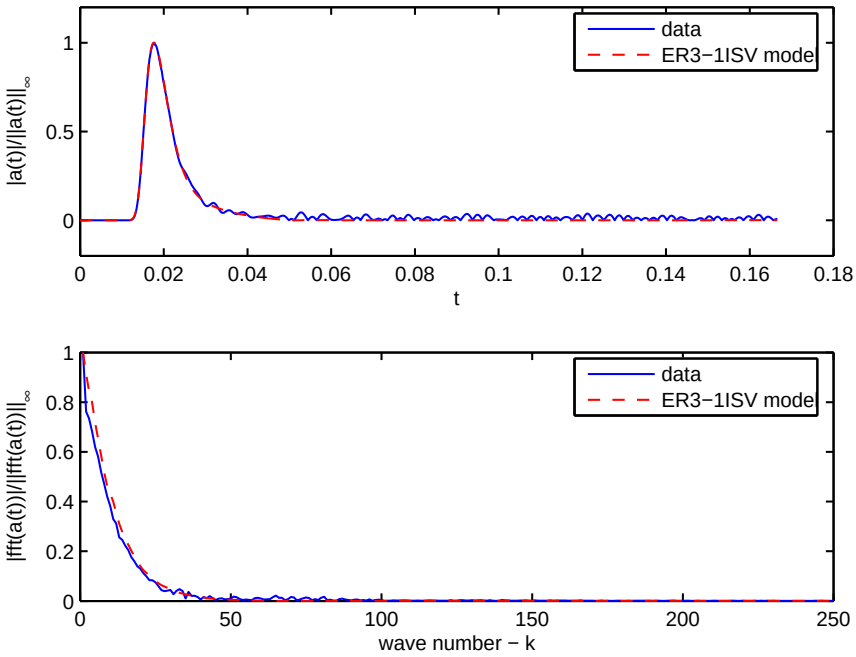

Figure 8: Optimal parameters $(C_\lambda,\nu_\lambda,C_\mu,\nu_\mu,\alpha_1,\alpha_2,\alpha_4)$ = (1853.634,250.178,2462.783,2061.129,1.273,1.882, 0.661) in model ER3-1ISV vs. data.

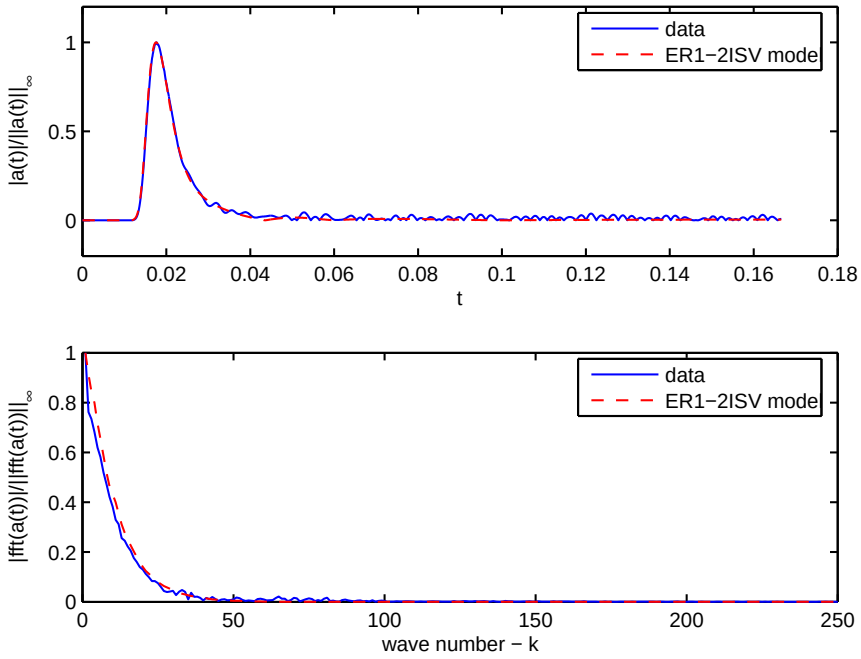

Figure 9: Optimal parameters $(C_{\lambda_1}, C_{\lambda_2}, \nu_{\lambda_1}, \nu_{\lambda_2}, C_{\mu_1}, C_{\mu_2}, \nu_{\mu_1}, \nu_{\mu_2}) = (1187.432, 1432.646, 215.841, 215.842, 386.639, 3456.749, 38.514, 2093.164)$ in model ER1-2ISV vs. data.

in each model. In all plots, the original data is given with a solid line; the optimized model solution is indicated with a dashed line. Clearly, models ER1-2ISV and ER3-1ISV produce better approximations to the data than the other models do.

5 Statistical model comparison

With the successful implementation of the four different versions of our model, it is natural to ask which model gives the best fit. We observe that as one adds increased complexity and detail in the models, one increases the number of parameters (i.e., degrees of freedom) to be estimated via the OLS optimization. One way to formulate the model comparisons is to question whether the additional parameters introduced in the more complicated models are significant in providing a better fit. Examination of the graphs of each model's simulation with optimal parameters in comparison to the data is not, by itself, a sufficient method of comparing the significance of additional parameters to our modelling efforts. For this reason, we will use a statistical test described and used in [11]. This method involves the examination of two models with parameter sets $\tilde{Q}$ and Q_0, where $Q_0 \subset \tilde{Q}$ in a way that the degrees of freedom associated with Q_0 is less than that of $\tilde{Q}$. In our case this will occur by fixing some of the parameter values in $\tilde{Q}$ at zero to obtain the set Q_0. Using an OLS minimization routine, one finds $\hat{q} \in Q_0$ and $\bar{q} \in \tilde{Q}$, such

Table 4: χ^2 values.

DOF	$\alpha=.10$	$\alpha=.05$	$\alpha=.01$	$\alpha=.001$
1	$\tau=2.71$	$\tau=3.84$	$\tau=6.63$	$\tau=10.8$
2	$\tau=4.61$	$\tau=5.99$	$\tau=9.21$	$\tau=13.8$
3	$\tau=6.25$	$\tau=7.81$	$\tau=11.3$	$\tau=16.3$
4	$\tau=7.78$	$\tau=9.49$	$\tau=13.3$	$\tau=18.5$

that $\hat{q}$ and $\bar{q}$ minimize the functional

$$J(q)=\sum_{i=1}^{N}|a(t_i;q)-a_i^d|^2,$$

over their respective parameter sets Q_0 and $\tilde{Q}$. Here a_i^d is the measured data, $a(t_i;q)$ is the model approximation, and N is the number of data points used in the data set $\{a_i^d\}$. For each of the statistical significance tests which we present here, there were 2048 data points, so $N=2048$.

We use the values $J(\hat{q})$ and $J(\bar{q})$ to create a test statistic U_N defined as

$$U_N=N\frac{J(\hat{q})-J(\bar{q})}{J(\bar{q})}.$$

We are then ready to test the significance of the extra parameters used in the model formulated with parameter set $\tilde{Q}$. We formulate a null hypothesis, that the correct parameter is $\hat{q}\in Q_0$. As summarized in [11], it is shown in [8] under standard (and reasonable) assumptions that as N tends to ∞, the test statistic U_N approaches a χ^2 distribution with degrees of freedom equal to the difference in degrees of freedom in $\tilde{Q}$ and Q_0 . Thus, we compare the test statistic to values from a χ^2 table (e.g., see Table 4) with the degrees of freedom equal to the difference in the number of parameters over which we optimize in the two sets. If our test statistic U_N is greater than the τ value in the χ^2 table for a given α, then the test suggests that we reject the null hypothesis with a $(1-\alpha)\times 100\%$ confidence level. The statistical model comparison results can thus be presented for various models, including the model presented in [6].

5.1 2 dimensional model – ER1-1ISV vs. ER1-2ISV

We expect that the results from the 2 dimensional model should be similar to the results presented for the 1 dimensional model. Examination of Fig. 9 suggests that a model employing 2 internal strain variables gives a good fit to our data. Table 5 displays the parameter sets for the two models, and their corresponding optimal cost values. Using these cost values, we can compute the test statistic $U_N=85412.52$. Since the model employing two internal strain variables has 4 parameters more than the original model, we compare this test statistic with the χ^2 values in Table 4 for 4 degrees of freedom. Clearly,

Table 5: Data Comparison 2D ER1-1ISV vs. 2D ER1-2ISV.

	parameters	cost J
Q_0	$(C_\lambda,\nu_\lambda,C_\mu,\nu_\mu,0,0,0,0)$	$J(\hat{q})=18.47514$
$\tilde{Q}$	$(C_{\lambda_1},\nu_{\lambda_1},C_{\mu_1},\nu_{\mu_1},C_{\lambda_2},\nu_{\lambda_2},C_{\mu_2},\nu_{\mu_2})$	$J(\bar{q})=0.432619$

Table 6: Data Comparison 2D ER1-1ISV vs. 2D ER2-1ISV.

	parameters	cost J
Q_0	$(C_\lambda,\nu_\lambda,C_\mu,\nu_\mu,0)$	$J(\hat{q})=18.47514$
$\tilde{Q}$	$(C_\lambda,\nu_\lambda,C_\mu,\nu_\mu,a_3)$	$J(\bar{q})=18.46135$

Table 7: Data Comparison 2D ER1-1ISV vs. 2D ER3-1ISV.

	parameters	cost J
Q_0	$(C_\lambda,\nu_\lambda,C_\mu,\nu_\mu,0,0,0)$	$J(\hat{q})=18.47514$
$\tilde{Q}$	$(C_\lambda,\nu_\lambda,C_\mu,\nu_\mu,\alpha_1,\alpha_2,\alpha_4)$	$J(\bar{q})=0.4446687$

the test statistic is larger than the τ values for each α level, thus, we reject the null hypothesis at all confidence levels including that at 99.9%. This strongly suggests that the model employing 2 internal strain variables provides a statistically significant better fit to data than that of the original model.

5.2 2 dimensional model – ER1-1ISV vs. ER2-1ISV

In the original model, we assumed that E_{12} and E_{21} are negligible or equivalently that $a_3=0$. The model that incorporates the second elastic response assumes that $E_{12}=E_{21}\neq 0$, adding an extra parameter a_3 to the system. We wish to test this extra parameter for significance in the model. The parameter sets and optimal costs for the models employing ER1 and ER2 are presented in Table 6. With the optimal costs for each model, we can compute a test statistic $U_N=1.5298$. With only one additional parameter, we compare the test statistic to the τ values for $\chi^2(1)$ in Table 4. The test statistic is less than τ for all α values in the table, thus we accept the null hypothesis, that the extra model parameter, a_3, is not necessary.

5.3 2 dimensional model – ER1-1ISV vs. ER3-1ISV

Finally, we examine the assumption that we can ignore the small stress term in the elastic response. ER1 was formed with the assumption that it could be ignored, while ER3 was formed assuming that it was necessary to the model. The inclusion of the small stress term adds three additional parameters to the model. The parameters and optimal costs for each model formulation can be seen in Table 7. From the optimal costs, we compute a test statistic $U_N=82{,}920.87$, and we are ready to conduct the statistical test. Since there

are three additional parameters, we will compare the test statistic with the τ values of $\chi^2(3)$. The test statistic is significantly larger than the τ values at all levels of α, thus we can reject the null hypothesis at a 99.9% confidence level. This suggests that the model is better formulated with the inclusion of the small stress term when fitting to the data set under investigation.

5.4 Combining significant models

The preceding results lead us to believe that we get a better fit from the model employing the third elastic response, and also that incorporating 2 internal strain variables allows for an improved model. These results prompted us to consider combining the two models, that is, we now examine a model that utilizes two internal strain variables, along with the third elastic response. Fig. 10 displays a comparison of the acceleration data with the new model's approximation with optimal parameters. Examination of the graph reveals a good fit to the data, but it is hard to determine whether it is a "better" fit than that provided by the previous models.

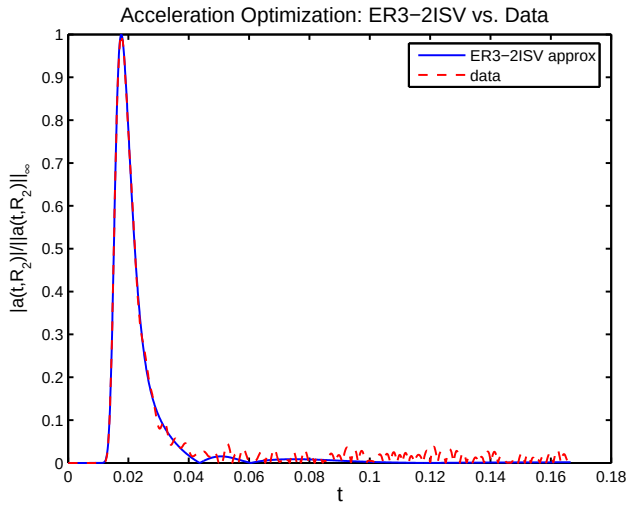

Figure 10: Comparison of 1D acceleration data to 2D approximation of acceleration computed using model ER3-2ISV.

Tables 8 and 9 display the optimal costs needed to compare the combined model with the individual models. Using the cost functionals in Table 8, we compute the test statistic to compare the model using two internal strain variables with the first elastic response to the model using two ISV's with the third elastic response. The test statistic will have value $U_N = 8.747$. Comparison of this test statistic with the $\chi^2(3)$ table, we see that the extra parameters are statistically significant at a 90% confidence level but not at a 95% level.

Similarly, examination of Table 9 leads us to the test statistic $U_N = 66.075$ for the comparison of ER3-1ISV vs. ER3-2ISV. We use the $\chi^2(4)$ values to conduct the hypothesis

Table 8: Data Comparison ER1-2ISV vs. ER3-2ISV.

	parameters	cost J
Q_0	$(C_{\lambda_1},\nu_{\lambda_1},C_{\mu_1},\nu_{\mu_1},C_{\lambda_2},\nu_{\lambda_2},C_{\mu_2},\nu_{\mu_2},0,0,0)$	$J(\hat{q})=0.43261$
$\tilde{Q}$	$(C_{\lambda_1},\nu_{\lambda_1},C_{\mu_1},\nu_{\mu_1},C_{\lambda_2},\nu_{\lambda_2},C_{\mu_2},\nu_{\mu_2},\alpha_1,\alpha_2,\alpha_4)$	$J(\bar{q})=0.430770$

Table 9: Data Comparison ER3-1ISV vs. ER3-2ISV.

	parameters	cost J
Q_0	$(C_{\lambda},\nu_{\lambda},C_{\mu},\nu_{\mu},0,0,0,0,\alpha_1,\alpha_2,\alpha_3)$	$J(\hat{q})=0.444668$
$\tilde{Q}$	$(C_{\lambda_1},\nu_{\lambda_1},C_{\mu_1},\nu_{\mu_1},C_{\lambda_2},\nu_{\lambda_2},C_{\mu_2},\nu_{\mu_2},\alpha_1,\alpha_2,\alpha_4)$	$J(\bar{q})=0.430770$

testing, and we see that the extra parameters are statistically significant for all confidence levels. Because the transition from model ER1-2ISV to model ER3-2ISV only had a 90% confidence level in the statistical significance testing, and because ER3-2ISV is more computationally intensive than ER1-2ISV, we shall employ model ER1-2ISV for all simulations presented in the remainder of our discussions.

6 Simulation results

In this section, we consider various modifications (e.g., constitutive assumptions, geometry, etc.) of the model to deal with different situations which are of interest when modelling wave propagation in biotissue. Since we previously established that the model employing the first elastic response, with two internal strain variables was one of the more useful (from computational as well as characterization considerations) versions of our model, all results reported within this section have been generated using the model ER1-2ISV.

6.1 The importance of viscoelasticity in modelling efforts

Although we have derived our model under the tacit assumption that biotissue has viscoelastic properties, there are other groups conducting research in this field that utilize constitutive equations related to *elastic* media for their modelling efforts [24, 25, 32]. This raises the question as to whether the more complicated viscoelastic models, as proposed by Fung and others, really are needed to accurately characterize biotissue. We therefore examined the difference between a model employing an elastic assumption and one which assumes viscoelasticity. The Maxwell, Voigt, and Kelvin models for viscoelasticity are rather easily reduced to an elastic model by setting the viscous portion to be equal to zero. Similarly, we can reduce our model to a purely elastic model with little difficulty.

When we derived our model using the internal strain variables, we defined

$$\lambda(t)=C_{\lambda}e^{-\nu_{\lambda}t};\quad \mu(t)=C_{\mu}e^{-\nu_{\mu}t},$$

and used the parameters λ and μ to define the reduced relaxation function. These exponentials are sometimes written as $Ce^{-t/\tau}$ where the parameter τ represents the relaxation time for the material. Therefore our relaxation parameter ν is equivalent to $\frac{1}{\tau}$, i.e., ν is the inverse of the relaxation time τ. If a material is purely elastic, it does not exhibit relaxation so that the corresponding relaxation time approaches ∞. We can reduce our model from a viscoelastic model to an elastic model by defining

$$\nu = \lim_{\tau\to\infty} \frac{1}{\tau} = 0.$$

To examine the effect of ν on our system, we ran simulations with values of $10\nu_k^*, \nu_k^*, \nu_k^*/10, \nu_k^*/50$, and $\nu_k = 0$, where the ν_k^*'s represent the optimized parameters for the ER1-2ISV model.

All simulations and boundary conditions were treated in the same manner as before, and we used the modified input function depicted in Fig. 11 to define the prescribed boundary condition for w_1. This modified input is identical to the original input depicted in Fig. 5, except it has been shifted so that its steady state occurs at zero.

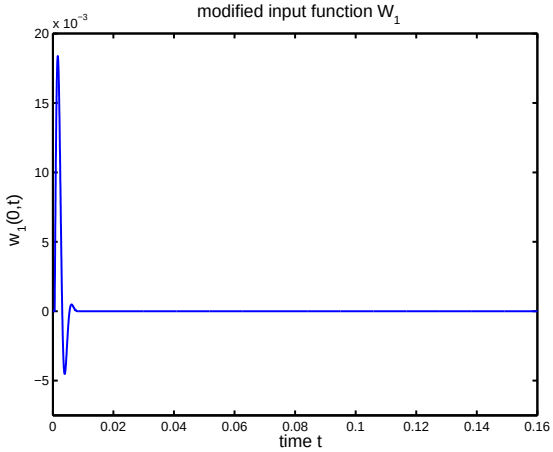

Figure 11: Modified input function with zero steady state.

Fig. 12 displays time snapshot results for v_1 for each value of ν at various time steps. The full animations from which these snapshots were taken are available at the website [1].

Examination of snapshots in Fig. 12 reveals the effect of the relaxation parameters on the model. From these figures, we note that as time increases, the results produced using larger values for the relaxation parameter exhibit more dissipation, and approach a steady state more rapidly. When $\nu = 10\nu_k^*$, we observe that the wave has almost completely dissipated in a short period of time (depicted in Fig. 12 (top)). It takes longer for the $\nu_k^*/10$ solution to dissipate completely, and although the result from the simulation using $\nu_k^*/50$ doesn't completely dissipate in the time frame shown in our figures, the amplitude of its wave has obviously been reduced in comparison to the $\nu = 0$ simulation.

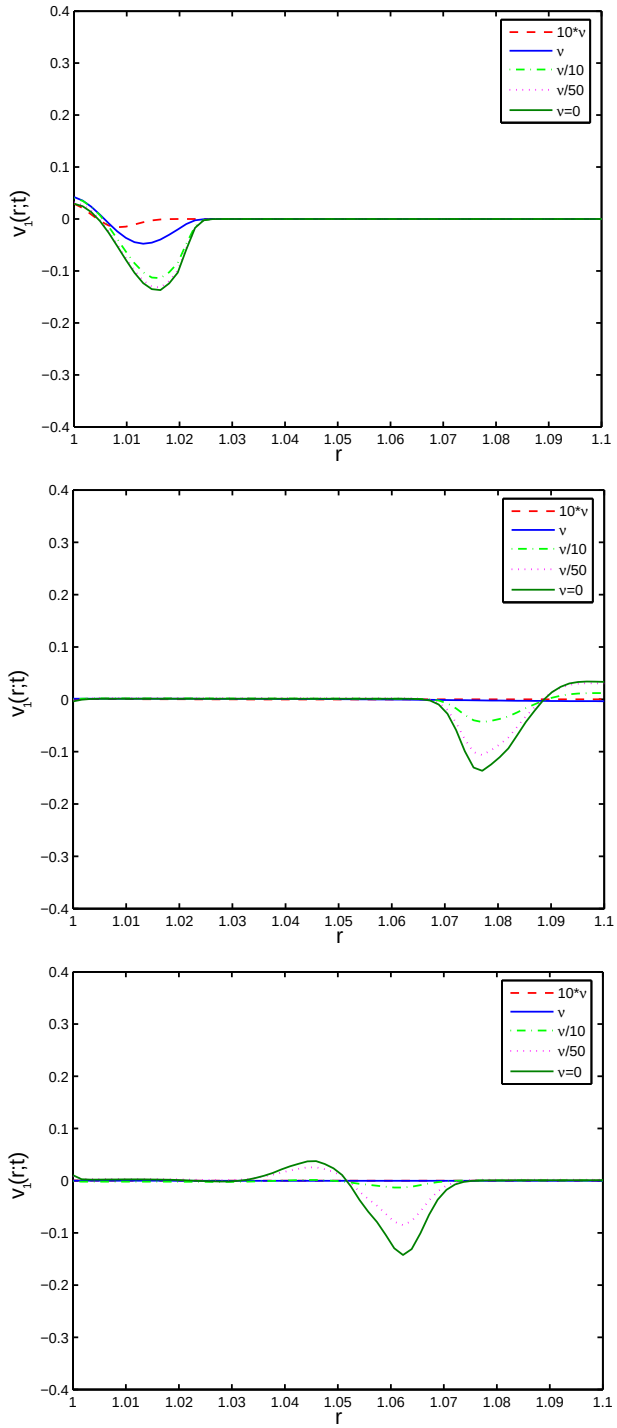

Figure 12: Results for v_1 for varying values of the relaxation parameter, ν, at t=0.0032 (top); t=0.0146 (middle); t=0.0325 (bottom).

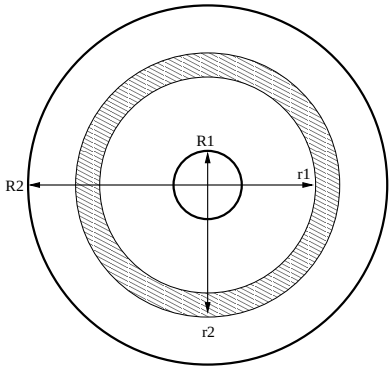

Figure 13: Model Geometry with a uniform ring of a different material.

When we set $\nu=0$, we see no dissipation in the amplitude of the wave. The wave simply reflects from one boundary to the other, traveling back and forth like a pendulum. This is what we would expect when dealing with an elastic medium. Thus, our results validate our assumption that setting $\nu=0$ effectively reduces our model from viscoelastic in nature to elastic.

While our results demonstrate that our model can be easily reduced to an elastic model, they also suggest that the results produced by an elastic model vary significantly from the results generated by a model incorporating viscoelasticity. Because we know dissipation occurs in biomaterials, the viscoelastic model clearly is a more realistic model. We must conclude that inverse or interrogation methodology based on elastic models (with no dissipation) may not be particularly useful when used with data from dissipative materials. The difference between the elastic and viscoelastic propagations motivate our efforts in using a viscoelastic approach to modelling wave propagation in biotissue.

6.2 Investigating a heterogeneous annular medium

To this point, all of our modelling efforts have been conducted in a homogeneous geometry. This, of course, is the simplest type of geometry to consider but is not particularly useful for the interrogation problems of interest here. For our application (the detection of CAD), we are interested in waves traveling through the chest cavity which we know is not a homogeneous medium. It is comprised of general biotissue, lung tissue, bone, cartilage, and other materials. To incorporate heterogeneity into our geometry we begin with the simplest possible situation and, motivated by human physiology including a rib cage and layers of chest/back muscle, introduce a ring comprised of one of the different materials in the middle of our original geometry. This is illustrated in Fig. 13.

We consider rings comprised of materials with different properties: a highly dense, purely elastic material; a medium density, slightly viscoelastic material; and a low density, highly viscoelastic material. The determination of suitable parameter values for the different materials from the available literature is a daunting task. While parameter val-

Table 10: Parameter values used in heterogeneous model simulations.

	homogeneous	mid dens-low visc	low dens-high visc	high dens-purely elas
C_{λ_1}	1187.432	726.943	1421.623	713.623
ν_{λ_1}	215.841	1.961	2857.14	0
C_{λ_2}	1432.646	978.193	1873.444	824.172
ν_{λ_2}	215.841	1.852	2860.7	0
C_{μ_1}	386.639	213.72	405.2	24.991
ν_{μ_1}	38.514	16.667	100.023	0
C_{μ_2}	3456.749	2980.75	3560.827	1872.634
ν_{μ_2}	2093.164	158.73	7299.27	0

ues are readily available for various types of materials, almost all parameters (e.g., elastic modulus, Lamé constants, etc.) reported are representative of the material as a whole and not those associated with the internal variables on which we have based our model. Thus, the parameter values reported throughout the literature are of little direct use in our modelling efforts. In order to obtain parameter values suitable to our needs, we begin with values presented in literature and manipulate the parameter values until they produce results which are commensurate with our expectations.

To gain an understanding of how each parameter affects the propagation simulations, we examined the results produced by changing one parameter at a time (while keeping all others set to their original value). We examined the results generated by increasing as well as decreasing each parameter. We find as expected that the parameters ν_{λ_1}, ν_{λ_2}, and ν_{μ_1} directly impact the rate of dissipation in the model. When these parameters are increased, the amplitude of the resulting wave dissipates more quickly, and dissipation occurs more slowly when these parameters are decreased. The parameter ν_{μ_2} does not appear to affect dissipation in the same manner as the other ν parameters. It does, however, seem to have an inverse relationship to the initial amplitude and wave propagation speed. Investigation of the parameters C_{λ_1}, C_{λ_2}, and C_{μ_1} reveals that an increase in the parameter value results in an increase in both the initial amplitude and propagation speed. The parameter C_{μ_2} also causes an increase in amplitude and propagation speed when the parameter value is increased, but it also seems to directly affect the rate of dissipation.

Using this knowledge of how each parameter affects the simulations of our model, we are able to manipulate the parameter values so that the resulting simulations exhibit behaviors meeting desired features. Table 10 displays parameter values used to generate such results for several different types of materials characterized by their density and viscoelasticity/elasticity properties.

Having determined parameter values which produce the appropriate characteristics for each type of material, we then examined the model with a ringed geometry. As depicted in Fig. 13, we prescribe a uniform ring throughout the middle of our original geometry. As the wave travels through the annular geometry, it will begin by propagating

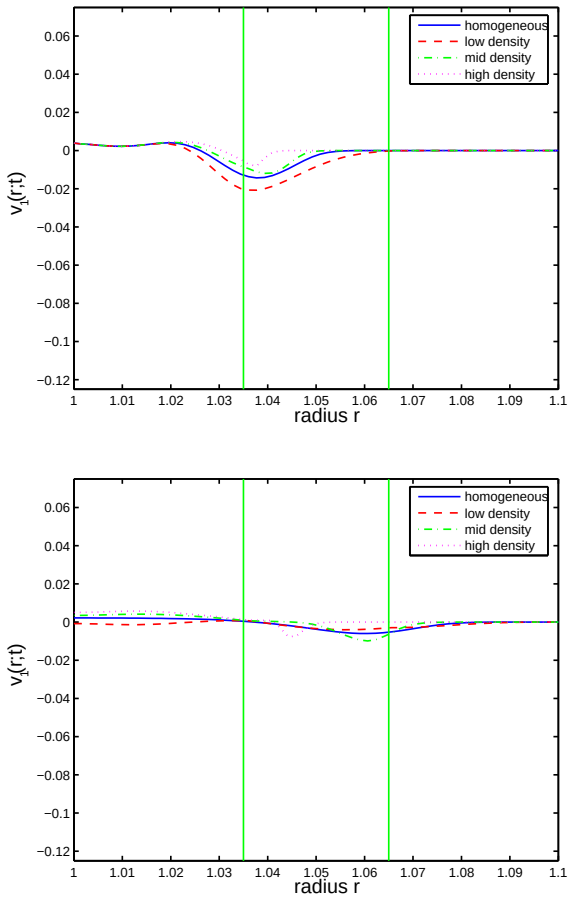

Figure 14: Results for v_1 for the ringed geometry, t=0.0081 (top); t=0.0121 (bottom).

in a biotissue region. It then encounters the ring of a different material, and after traveling through the ring, it will pass again into a region of biotissue medium.

While traveling through the various media, we expect the properties of the wave when it enters and exits the ring to exhibit the behavior of transmissions and reflections across a general interface as described in [2]. When the wave travels from a material of higher density into one of lower density, the wave will be reflected as well as transmitted. The transmitted portion of the wave has an amplitude which is roughly half of what the incident wave was. The reflected portion has an amplitude comparable to the transmitted portion, but it has the opposite polarity. A wave moving from a material of lower density into one of higher density also will have a transmitted and reflected portion. The transmitted wave, in this scenario, is larger than the incident wave was, while the reflected wave is roughly half of the size of the incident wave. The reflected and transmitted waves have the same polarity.

Fig. 14 displays snapshots (again see [1] for movies) of the propagation of waves in a heterogeneous geometry. Even though the waves are 2-dimensional, the uniformity in θ of both the input signal and the geometry yields waves that are uniform in θ and hence readily depicted in "1-dimensional slices" in r for a fixed value of θ. In Fig. 14 (top), which depicts the waves after they have been introduced into annular regions with several different material components rings, we see that the wave traveling in the low density general biotissue material propagates with the fastest speed, and the wave introduced to the highly dense material has the slowest speed. Furthermore, we see that the wave traveling into the low density, highly viscoelastic material, a material with lower density than the general biotissue, has a transmitted portion with larger amplitude, and a reflected portion with the same polarity. Also, the waves which encounter the more dense materials (mid density and highly dense) have transmitted waves with smaller amplitudes, and reflected waves with opposite polarity. These observations are precisely what we would expect to see. As time increases (Fig. 14 (bottom)), we observe that the wave traveling through the ring of low density dissipates (almost completely), the wave traveling through the ring with medium density reflects off of the outer edge of the ring and dissipates as it travels. The wave traveling through the ring of highly dense, purely elastic material shows no dissipation, but every time it encounters the edge of the ring, part of its amplitude is transmitted, and the remainder is reflected back into the ring. As this occurs each time the wave interacts with the ring/biotissue interface, the amplitude of the wave inside of the annular ring geometry is slowly decreasing, and will eventually disappear.

6.3 Incorporating a θ dependency representing a partial occlusion

In each example that we have examined to this point, our models have been independent of the variable θ. Essentially, this means that all models that we have considered can be reduced to a one dimensional model. As an initial attempt to introduce the θ dependency, we begin with our original geometry. We assume that a buildup of plaque (cholesterol, calcium, and platelets) has formed along the wall of the inner radius of our geometry as depicted schematically in Fig. 15. We assume that this buildup is completely rigid and impermeable, thus any impulse along the inner radius will have no effect on the region occluded by the buildup.

In order to numerically solve our system under these conditions, we define the impulse along the inner radius as follows:

$$w_1(t;R_1,\theta) = f_1(t)s(\theta),$$

where $f_1(t)$ is the original impulse function, (depicted in Fig. 5) and $s(\theta)$ is defined as

$$s(\theta) = \begin{cases} 0, & \theta_1 \le \theta \le \theta_2, \\ 1, & \text{elsewhere.} \end{cases} \tag{6.1}$$

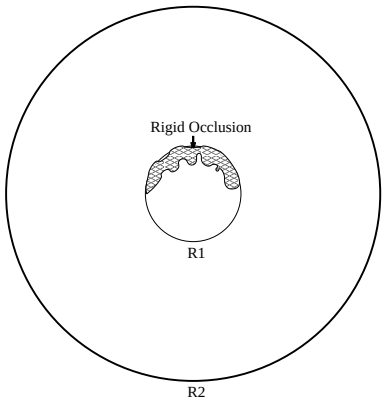

Figure 15: Geometry with occlusion along inner radius.

This is clearly a rather simple approximation to the geometry that an occlusion in an artery will generally produce, but serves to illustrate expected wave behavior in such situations. For our computational efforts here, we assumed that the occlusion affects the area between $\theta_1 = 3\pi/8$ and $\theta_2 = 5\pi/8$. Computations were again carried out using the MacCormack scheme, and boundary values were once again updated using direction cosines. However, our input function, $w_1(t;R_1,\theta)$, as defined above, has discontinuities at the edges of the occlusion (θ_1 and θ_2). These discontinuities cause difficulties with the integration scheme, and must be treated with certain precautions [23, 30]. Although the method of direction cosines allows one to prescribe only one boundary condition (corresponding to the one eigendirection that points into the domain) on the inner radius, the presence of discontinuities in the input permits one to prescribe additional conditions. To ensure that the problem is well defined, one can define the velocity across the discontinuity. In [23], Hirsch notes that in this situation, we should define the tangential velocity to be zero across the discontinuity. This means that we may prescribe

$$v_2(t;R_1,\theta_1 \pm \epsilon) = 0, \quad v_2(t;R_1,\theta_2 \pm \epsilon) = 0$$

for arbitrarily small ϵ. We carried out our simulation using the discontinuous impulse function, as well as this new boundary condition, and snapshots of our results are displayed in Fig. 16 (again, movies can be found at [1]).

The graphs in the left sides of Fig. 16 depict the radial velocity v_1 throughout the geometry at successive times. Note that the velocity propagates outward uniformly, with the exception of the area of the occlusion. Examining the right graphs of Fig. 16, we see that velocity v_2 in the tangential direction is nontrivial only on the border at the occlusion along a line in the radial direction. This is what we should expect, because this is the only place where a dependency on θ exists. The results shown in Fig. 16 might suggest that there is little happening in the sector of the geometry affected by the occlusion but this is not the case. The velocity in the rest of the geometry diffuses into the portion of the geometry affected by the occlusion even though the values of the velocity in the affected

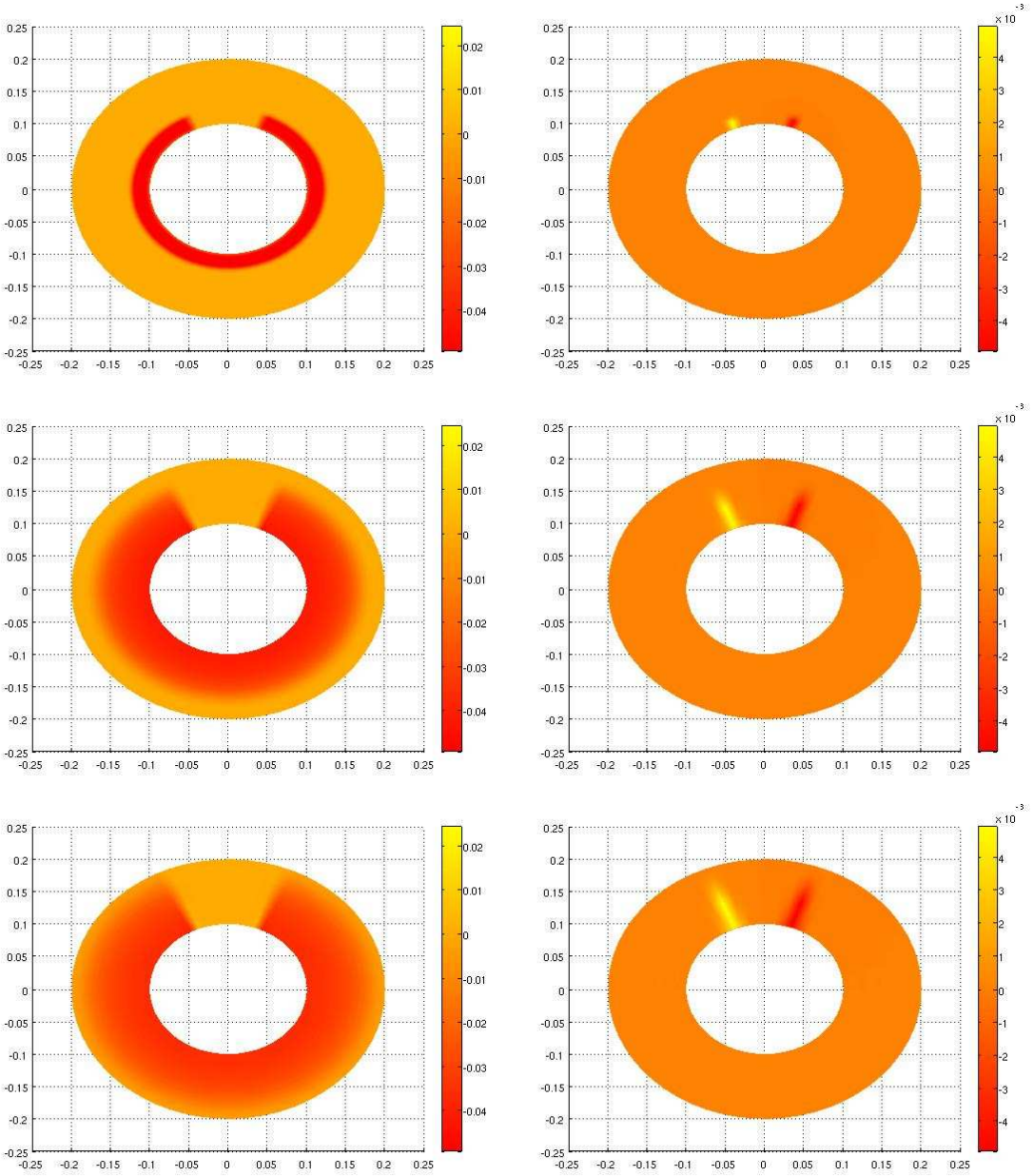

Figure 16: Values for v_1 (left) and v_2 (right) for the geometry with an occluded inner radius, at successive times t=0.0039 (top), t=0.0121 (middle), and t=0.0162 (bottom).

region are several orders of magnitude smaller than that in the rest of the medium and hence is not discernable at the resolutions in Fig. 16. Plots at a finer resolution clearly depicting and confirming this can be found in [31].

6.4 Combining the ringed geometry and the θ dependent occlusion

Having demonstrated the ability to separately incorporate heterogeneities and theta dependencies into our model, we next combined these components into one model. We consider a geometry with a heterogeneous ring running around the middle of the annulus and a hard occlusion blocking a portion of the inner radius of the annulus. We once again define the ring by modifying the material parameters of our model as described in Section 6.2. The dynamics of the occlusion will be treated as in Section 6.3. We used the input function which attains a steady state of zero (depicted in Fig. 11), which allows one to observe reflection and transmission behavior at the ring/biotissue interface. If this model is implemented correctly, the expected observations should be a combination of those from the two models separately. We expect to see little activity in the portion of the geometry affected by the occlusion. Reflected and transmitted waves should be observable, and they should behave as previously described. We first examine the model including a ring of highly dense, purely elastic material. Snapshots (from movies in [1]) for the radial velocity, $v_1(t;r,\theta)$, are presented in Fig. 17 for successive times.

From Fig. 17 (top), we see that upon encountering the interface with the ring, the v_1 wave is both transmitted and reflected. As expected, the reflected portion of the wave changes polarity and the portion which is transmitted displays a slower propagation speed and a considerably smaller wavelength. The behavior of transmitted and reflected portions of our wave is again displayed in Fig. 17 (middle) and (bottom). While dissipation does not occur within the ring, we do note that the activity occurring within the ring is reducing as time progresses. Each time that the portion of the wave traveling within the ring encounters an interface with the general biotissue, it is reflected and transmitted, causing a reduction in its amplitude. Successive interactions with the ring/general biotissue boundary causes the energy of the wave to decrease and eventually vanish.

Investigating the v_2 graphs in Fig. 17, we observe that the only places where the tangential velocity is nonzero is at the boundaries of the occlusion along the inner radius ($\theta=3\pi/8$ and $\theta=5\pi/8$). It is interesting to note that, unlike the original occluded model, there doesn't appear to be much tangential activity occurring within the highly dense, purely elastic ring. Also, in our original results, the tangential velocity appeared to reflect (almost simultaneously) from the inner and outer radius, displaying a change in polarity. This same phenomenon occurs between the inner radius of our geometry and the ring, as well as between the ring and the outer radius.

We next examined an occluded geometry with a ring comprised of a material which is slightly more dense (1900 kg/m^3) and less viscoelastic than the general biotissue. Snapshots for the velocity values from movies [1] for this model can be viewed in Fig. 18. Because we established that the wave propagation in the general biotissue, before encountering the ring, will be the same regardless of ring material, our first depicted result Fig. 18 (top)) is of the initial interaction between the wave and the ring. As in the results presented in Fig. 17, we see a reflection of opposite polarity emanating from the biotissue/ring interface. Upon reaching the outer boundary of the ring (see Fig. 18 (bottom)),

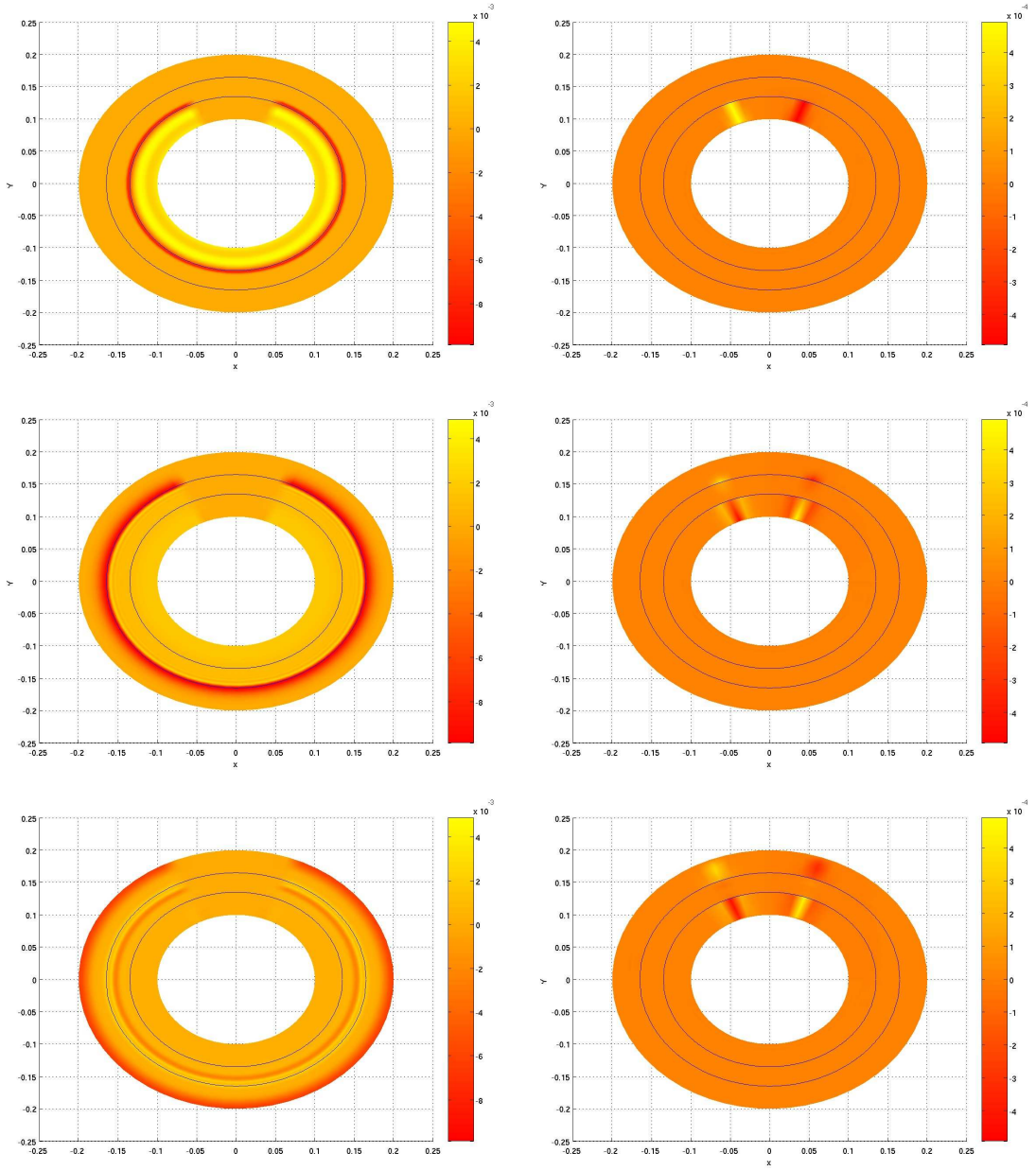

Figure 17: Values for v_1 (left) and v_2 (right) in an occluded geometry with a highly dense, purely elastic ring, at successive times $t=0.0081$ (top), $t=0.0223$ (middle), and $t=0.0284$ (bottom).

the wave is once again reflected and transmitted. The reflection in this instance is much weaker than that observed in our previously presented results. This can be attributed to the viscoelasticity of the material comprising the ring. Because the entire geometry has

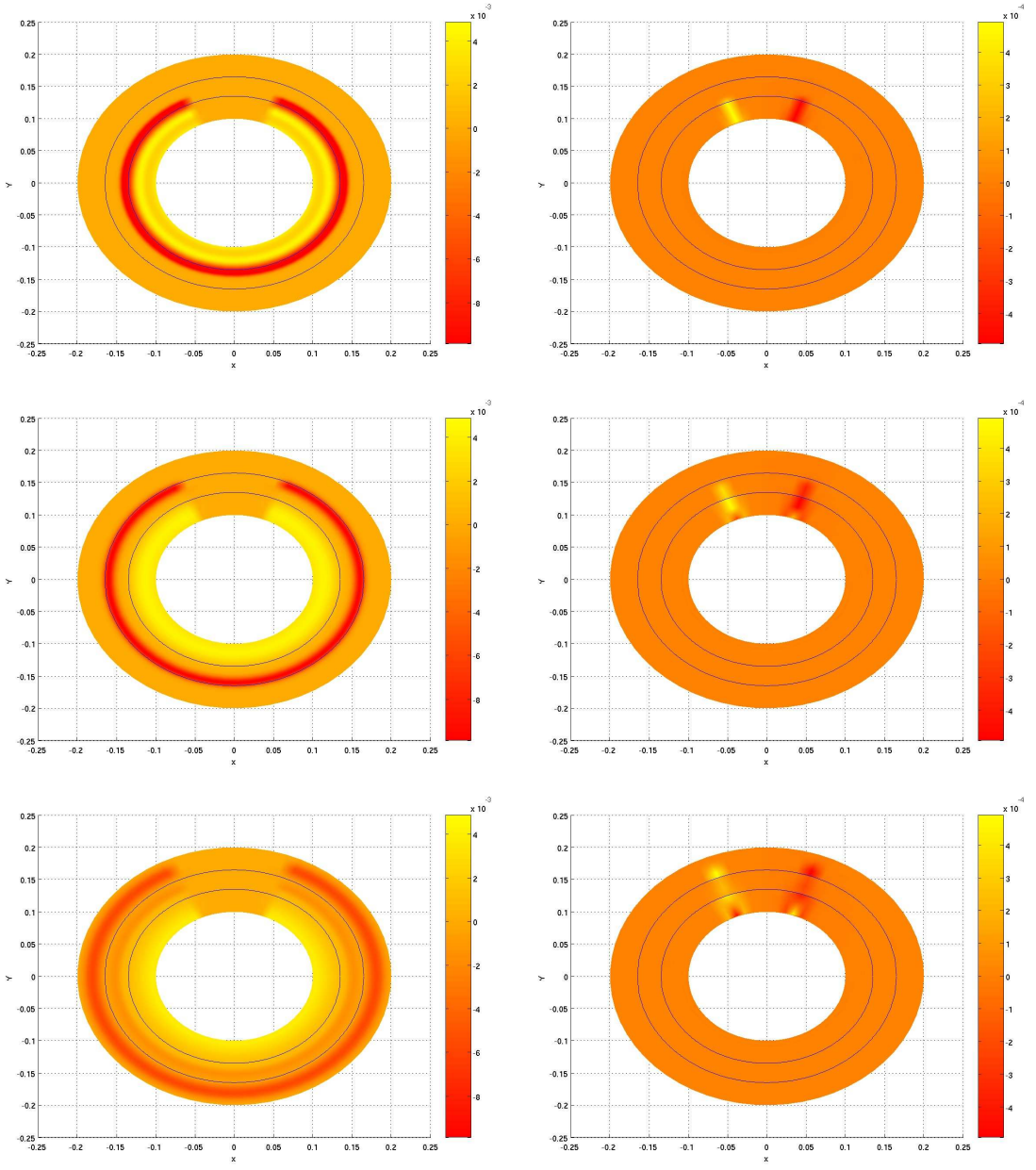

Figure 18: Values for v_1 (left) and v_2 (right) in an occluded geometry with a slightly more dense, less viscoelastic ring, at successive times t=0.0081 (top), t=0.0121 (middle) and t=0.0162 (bottom).

some degree of viscoelasticity, dissipation occurs throughout, and the observed activity appears to cease at an earlier time than in the previously considered model. The tangential velocity, shown in the rightmost graphs of Fig. 18, appears to behave in a manner

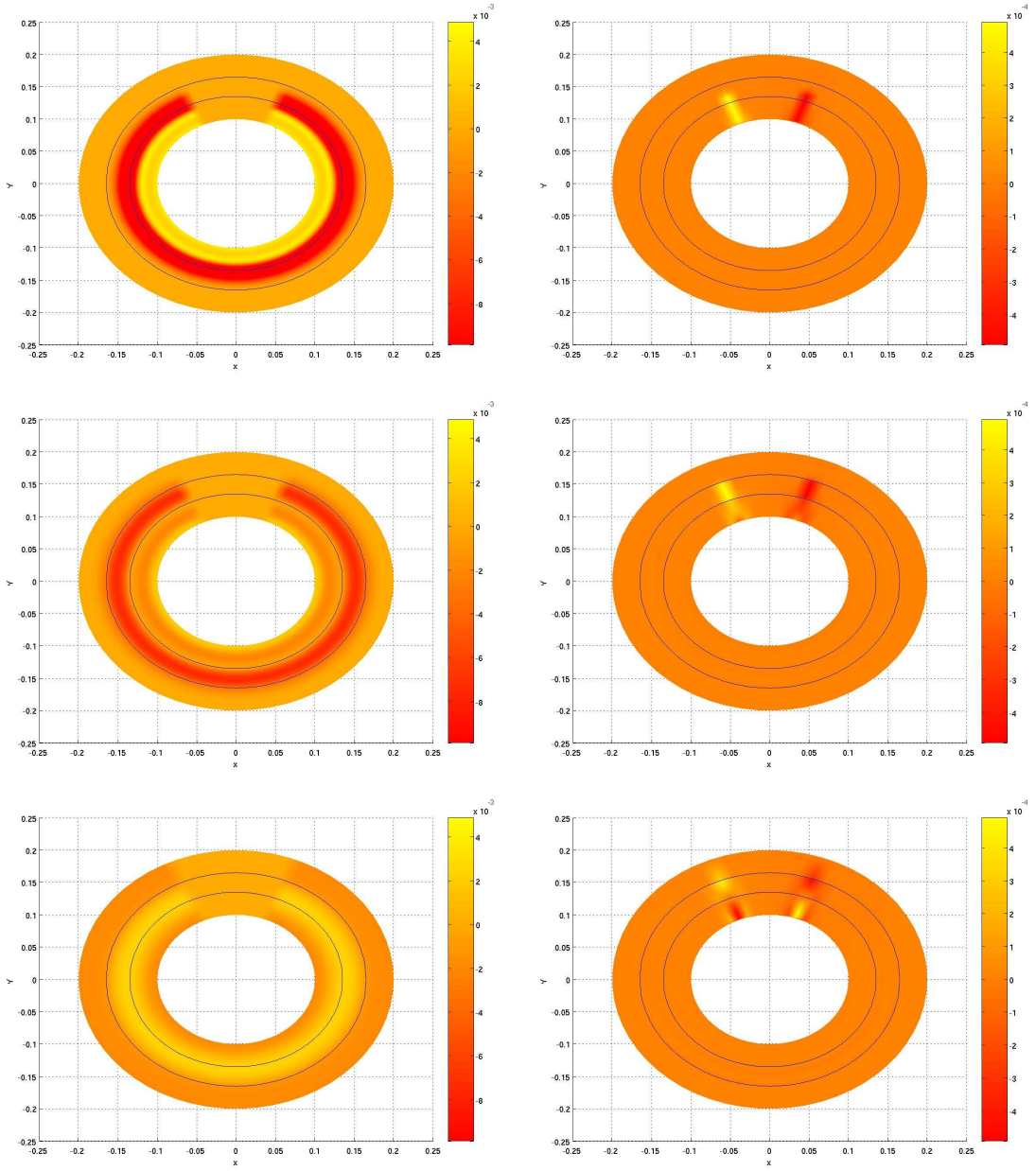

Figure 19: Values for v_1 (left) and v_2 (right) in an occluded geometry with a less dense, more viscoelastic ring, at successive times t=0.0081 (top), t=0.0121 (middle) and t=0.0162 (bottom).

similar to that in the previous model. Activity occurs along the boundary of the occlusion, and there appears to be a simultaneous reflection between the inner radius of the geometry and the inner radius of the ring.

Finally, we examined an occluded geometry with a ring formed of a material which is less dense, and more viscoelastic than the surrounding biotissue. Snapshots from the movies [1] of the resulting velocities from this model are presented in Fig. 19. Unlike the two previously considered scenarios, the reflection from the initial interaction with the material of the ring has the same polarity as the transmitted portion of the wave. This is what we would expect of a wave traveling from a material into one with a lower density. It should be pointed out that since this geometry is comprised of materials which are more viscoelastic than the previous models, the amplitude of our wave dissipates more quickly. The tangential velocity exhibits the same behavior as in the previous models, with the exception that it appears to dissipate more quickly (the wave is not as prevalent at t=0.0223 s, as it was in the previous models).

7 Concluding remarks and future directions

We have developed a mathematical framework to model the propagation of shear waves through biological tissue. Using previously published one dimensional results as a basis of comparison, we were able to examine the utility and appropriateness of our model, and we determined which variation of the model was best suited to the data by employing the statistical significance testing methodology outlined in [11]. More specifically, we have demonstrated model capabilities to distinguish between elastic and viscoelastic materials as well as to properly partially transmit and partially reflect at material interfaces. We have also computationally verified the ability to use the model to observe stenoses-like substructures (partial occlusions) via surface shear waves propagated from pulse-like internal disturbances.

After examining the appropriateness of our model, we presented a variety of simulations. We demonstrated the importance of incorporating viscoelasticity in modelling efforts. Our simulation involving a ringed geometry met our expectations, displaying the behavior of a wave that encounters an interface with a material with different properties. The simulation of the wave propagating from an inner radius with a rigid occlusion also performed as expected. The simulations presented within this document should easily be extended to consider more complicated geometries (i.e., nonuniform ring in geometry, multiple rings, multiple occlusions, etc.), which may be of interest in future investigations on this subject.

While the methods and results reported within this paper are a considerable extension of the project originally presented in [6], there are still several things to be done to reach the ultimate goal of stenosis detection. First, the modelling could be readily improved by considering more realistic formulations of the stenoses (e.g., a smoothed geometry in place of the discontinuous representation of (6.1)). We need to develop an inverse problem methodology (including a statistical OLS or Generalized Least Squares framework that permits longitudinal data with nonconstant variance) that facilitates the detection as well as characterization of stenoses. This methodology could also be used to identify

basic parameters for internal variables in healthy biotissue. To allow for a wider range of materials, we need to implement a probabilistic multi-scale approach to our model similar to that presented in [14]. A well-posedness (existence, uniqueness, and continuous dependence) framework should be investigated. Finally, we need to extend the model and methodology to accommodate a three dimensional geometry with axial variation in the stenosis.

Acknowledgments

This research was supported in part by the U.S. Air Force Office of Scientific Research under grant AFOSR-FA9550-04-1-0220 and in part by The David and Lucille Packard Foundation. The authors would like to express their appreciation to Dr S. Wynne-Verkruysse for valuable comments and suggestions throughout the course of this research.

References

[1] http://www.ncsu.edu/crsc/reports/reports06.htm — CRSC-TR06-28.
[2] http://www.kettering.edu/∼drussell/Demos/reflect/reflect.html
[3] http://www.texheartsurgeons.com/cad.htm
[4] R. Aris, Vectors, Tensors, and the Basic Equations of Fluid Mechanics, Dover Publications, New York, 1989.
[5] R. L. Bagley, A theoretical basis for the application of fractional calculus to viscoelasticity, J. Rheol., 27 (1983), 201-210.
[6] H. T. Banks, J. H. Barnes, A. Eberhardt, H. Tran and S. Wynne, Modeling and computation of propagating waves from coronary stenoses, Comput. Appl. Math., 21 (2002), 767-788.
[7] H. T. Banks and K. L. Bihari, Modeling and estimating uncertainty in parameter estimation, CRSC-TR99-40, NCSU, August, 1999; Inverse Probl., 17 (2001), 1-17.
[8] H. T. Banks and B. G. Fitzpatrick, Statistical methods for model comparison in parameter estimation problems for distributed systems, CAMS Tech. Rep. 89-4, University of Southern California, September, 1989; J. Math. Biol., 28 (1990), 501-527.
[9] H. T. Banks and N. L. Gibson, Well-posedness in Maxwell systems with distributions of polarization relaxation parameters, CRSC-TR04-01, NCSU, January, 2004; Appl. Math. Lett., 18 (2005), 423-430.
[10] H. T. Banks and N. L. Gibson, Electromagnetic inverse problems involving distributions of dielectric mechanisms and parameters, CRSC-TR05-29, NCSU, August, 2005; Q. Appl. Math., 64 (2006), 749-795.
[11] H. T. Banks and K. Kunisch, Estimation Techniques for Distributed Parameter Systems, Birkhäuser, Boston, 1989.
[12] H. T. Banks, N. G. Medhin and G. A. Pinter, Multiscale considerations in modeling of nonlinear elastomers, CRSC-TR03-42, NCSU, October, 2003; J. Comput. Meth. Sci. Eng., 8 (2007), 1-10.
[13] H. T. Banks, N. G. Medhin and G. A. Pinter, Nonlinear reptation in molecular based hysteresis models for polymers, Q. Appl. Math., 62 (2004), 767-779.
[14] H. T. Banks and G. A. Pinter, A probabilistic multiscale approach to hysteresis in shear wave propagation in biotissue, Multiscale Model. Simul., 3 (2005), 395-412.

[15] H. T. Banks, G. A. Pinter, L. K. Potter, M. J. Gaitens and L. C. Yanyo, Modeling of quasi-static and dynamic load responses of filled viscoelastic materials, CRSC-TR98-48, NCSU, December, 1998; in: E. Cumberbatch and A. Fitt (Eds.), Mathematical Modeling: Case Studies from Industry, Cambridge University Press, 2001, pp. 229-252.
[16] J. Bercoff, S. Shaffai, M. Tanter, L. Sandrin, S. Catheline, M. Fink, J. L. Gennison and M. Meunier, In vivo breast tumor detection using transient elastography, Ultrasound Med. Biol., 29 (2003), 1387-1396.
[17] A. P. Boresi and R. J. Schmidt, Advanced Mechanics of Materials, John Wiley & Sons, New York, 2003.
[18] S. Catheline, J.-L. Gennisson and M. Fink, Measurement of elastic nonlinearity of soft solid with transient elastography, J. Acoust. Soc. Am., 114 (2003), 3087-3091.
[19] Y. C. Fung, Biomechanics: Mechanical Properties of Living Tissues, Springer-Verlag, New York, 1993.
[20] J. E. Galbraith, M. L. Murphy and N. de Soyza, Coronary angiogram interpretation. Interobserver variability, JAMA, 240 (1978), 2053-2056.
[21] J. F. Greenleaf, M. Fatemi and M. Insana, Selected methods for imaging elastic properties of biological tissues, Annu. Rev. Biomed. Eng., 5 (2003), 57-78.
[22] R. G. Haut and R. W. Little, A constitutive equation for collagen fibers, J. Biomech., 5 (1972), 423-430.
[23] C. Hirsch, Numerical Computation of Internal and External Flows, Volume 2, John Wiley & Sons, Chichester, England, 1990.
[24] L. Ji and J. McLaughlin, Recovery of the Lamé parameter μ in biological tissues, Inverse Probl., 20 (2004), 1-24.
[25] L. Ji, J. McLaughlin, D. Renzi and J-R Yoon, Interior elastodynamics inverse problems: shear wave speed reconstruction in transient elastography, Inverse Probl., 19 (2003), S1-S29.
[26] J. Kevorkian, Partial Differential Equaitons: Analytical Solution Techniques, Wadsworth, Inc., California, 1990.
[27] R. C. Koeller, Applications of fractional calculus to the theory of viscoelasticity, J. Appl. Mech., 51 (1984), 299-307.
[28] M. Z. Kiss, D. E. Sayers, Z. Zhong, C. Parham and E. D. Pisano, Improved image contrast of calcification in breast tissue specimens using diffraction enhanced imaging, Phys. Med. Biol., 49 (2004), 3427-3439.
[29] M. Z. Kiss, T. Varghese and T. J. Hall, Viscoelastic characterization of in vitro canine tissue, Phys. Med. Biol., 49 (2004), 4207-4218.
[30] A. G. Kulikovskii, N. V. Pogorelov and A. Y. Semenov, Mathematical Aspects of Numerical Solution of Hyperbolic Systems, Chapman & Hall/CRC Press, Boca Raton, Florida, 2001.
[31] N. S. Luke, Modeling shear wave propagation in biotissue: An internal variable approach to dissipation, Ph.D. Dissertation, N. C. State University, 2006.
[32] J. R. McLaughlin and J-R Yoon, Unique identifiability of elastic parameters from time-dependent interior displacement measurement, Inverse Probl., 20 (2004), 25-45.
[33] S. E. Nissen and J. C. Gurley, Application of intravascular ultrasound for detection and quantitation of coronary atherosclerosis, Int. J. Card. Imaging, 6 (1991), 165-177.
[34] A. Pandit, X. Lu, C. Wang and G. S. Kassab, Biaxial elastic material properties of porcine coronary media and adventitia, Am. J. Physiol.–Heart Circ. Physiol., 288 (2005), H2581-H2587.
[35] J. G. Pinto and P. J. Patitucci, Viscoelasticity of passive cardiac muscle, J. Biomech. Eng., 102 (1980), 57-61.

[36] J. M. Price, P. J. Patitucci and Y. C. Fung, Mechanical properties of resting taenia coli smooth muscle, Am. J. Physiol.–Cell Physiol., 2 (1977), 047-055.
[37] E. P. M. Rousseau, A. A. H. J. Sauren, M. C. van Haut and A. A. van Steenhoven, Elastic and viscoelastic material behaviour of fresh and gluteraldehyde-treated porcine aortic valve, J. Biomech., 16 (1983), 339-348.
[38] L. Sandrin, D. Cassereau and M. Fink, The role of the coupling term in transient elastography, J. Acoust. Soc. Am., 115 (2004), 73-83.
[39] J. L. Semmlow, W. Welkowitz, J. Kostis and J. W. MacKenzie, Coronary artery disease correlates between diastolic auditory characteristics and coronary artery stenoses, IEEE T. Biomed. Eng., 30 (1983), 136-139.
[40] J. C. Strickwerda, Finite Difference Schemes and Partial Differential Equations, Wadsworth, Inc., California, 1989.
[41] B. Suki, A-L. Barabási and K. R. Lutchen, Lung tissue viscoelasticity: A mathematical framework and its molecular basis, J. Appl. Physiol., 76 (1994), 2749-2759.
[42] L. S. Taylor, M. S. Richards, A. J. Moskowitz, A. L. Lerner, D. J. Rubens and K. J. Parker, Viscoelastic effects in sonoelastography: Impact on tumor detectability, 2001 IEEE Ultrasonics Symposium, 2001, pp. 1639-1642.
[43] C. Verdier, Rheological properties of living materials: From cells to tissues, J. Theor. Med., 5 (2003), 67-91.
[44] S. L-Y. Woo, B. R. Simon, S. C. Kuei and W. H. Akeson, Quasi-linear viscoelastic properties of normal articular cartilage, J. Biomech. Eng., 102 (1980), 35-90.
[45] S. L-Y. Woo, M. A. Gomez and W. H. Akeson, The time and history dependent viscoelastic properties of the canine medial collateral ligament, J. Biomech. Eng., 103 (1981), 292-298.